A Geodynamic Investigation of Magma-Poor Rifting Processes and Melt Generation: A Case Study of the Malawi Rift and Rungwe Volcanic Province, East Africa

Emmanuel A. Njinju

Dissertation submitted to the Faculty of the
Virginia Polytechnic Institute and State University
in partial fulfillment of the requirements for the degree of

Doctor of Philosophy
in
Geosciences

D. Sarah Stamps, Chair
Scott King
Ying Zhou
Estella A. Atekwana

December 4, 2020
Blacksburg, Virginia

Keywords: Geosciences, Continental Rifting, Lithospheric-Modulated Convection,
Plume-Lithosphere Interactions, Melt Generation

A Geodynamic Investigation of Magma-Poor Rifting Processes and Melt Generation: A Case Study of the Malawi Rift and Rungwe Volcanic Province, East Africa

Emmanuel A. Njinju

(ABSTRACT)

Our understanding of how magma-poor rifts accommodate strain remains limited largely due to sparse geophysical observations from these rift systems. To better understand magma-poor rifting processes, chapter 1 of this dissertation is focused on investigating the lithosphere-asthenosphere interactions beneath the Malawi Rift, a segment of the magma-poor Western Branch of the East African Rift (EAR). Chapter 2 and 3 are focused on investigating the sources of melt beneath the Rungwe Volcanic Province (RVP), an anomalous volcanic center located at the northern tip of the Malawi Rift. In chapter 1, we use the lithospheric structure of the Malawi Rift derived from the World Gravity Model 2012 to constrain three-dimensional (3D) numerical models of lithosphere-asthenosphere interactions, which indicate $\approx 3\ cm/yr$ asthenospheric upwelling beneath the thin lithosphere (115-125 km) of the northern Malawi Rift and the RVP from lithospheric modulated convection (LMC) that is decoupling from surface motions. We suggest that the asthenospheric upwelling may generate decompression melts which weakens the lithosphere thereby enabling extension.

The source of asthenospheric melt for the RVP is still contentious. Some studies suggest the asthenospheric melt beneath the RVP arises from thermal perturbations in the upper mantle associated with plume head materials, while others propose decompression melting from upwelling asthenosphere due to LMC where the lithosphere is thin. Chapter 2 of this

dissertation is focused on testing the hypothesis that asthenospheric melt feeding the RVP can be generated from LMC using realistic constraints on the mantle potential temperature (T_p). We develop a 3D thermomechanical model of LMC beneath the RVP and the entire Malawi Rift that incorporates melt generation. We find decompression melt associated with LMC upwelling (≈3 cm/yr) occurs at a maximum depth of 150 km localized beneath the RVP.

Studies of volcanic rock samples from the RVP indicate plume signatures which are enigmatic since the RVP is highly localized, unlike the large igneous provinces in the Eastern Branch of the EAR. In chapter 3, we test the hypothesis that the melt beneath the RVP is generated from plume materials. We investigate melt generation from plume-lithosphere interactions (PLI) beneath the RVP by developing a 3D seismic tomography-based convection (TBC) model beneath the RVP. The seismic constraints indicate excess temperatures of $\approx 250K$ in the sublithospheric mantle beneath the RVP suggesting the presence of a plume. We find a relatively fast upwelling (≈10 cm/yr) beneath the RVP which we interpret as a rising plume. The TBC upwelling generates decompression melt (≈0.25 %) at a maximum depth of ≈200 km beneath the RVP where the lithosphere is thinnest (≈100 km). Our results demonstrate that an excess heat source from may be plume materials is necessary for melt generation in the sublithospheric mantle beneath the RVP because passive asthenospheric upwelling of ambient mantle will require a higher than normal T_p to generate melt.

A Geodynamic Investigation of Magma-Poor Rifting Processes and Melt Generation: A Case Study of the Malawi Rift and Rungwe Volcanic Province, East Africa

Emmanuel A. Njinju

(GENERAL AUDIENCE ABSTRACT)

Studies suggest the presence of hot, melted rock deep in the continents makes them weaker and easier to break apart, however, our understanding of how continents with less melted rock break apart remains limited largely due to sparse geophysical observations from these dry areas. To better understand how continents with less melted rock break apart, chapter 1 of this dissertation is focused on investigating the interactions between the rigid part of the Earth, called lithosphere, and the underlying lower viscosity rock layer called asthenosphere beneath the Malawi Rift, a segment of the magma-poor Western Branch of the East African Rift (EAR). Chapter 2 and 3 are focused on investigating the sources of melt beneath the Rungwe Volcanic Province (RVP), an anomalous volcanic center located at the northern tip of the Malawi Rift. In chapter 1, we use the lithospheric structure of the Malawi Rift derived from gravity data to constrain three-dimensional (3-D) numerical models of lithosphere-asthenosphere interactions, which indicate ≈ 3 cm/yr asthenospheric upwelling beneath the thin lithosphere (115-125 km) of the northern Malawi Rift and the RVP that does not seem to drive movements at the surface. We suggest that the asthenospheric upwelling may generate melted rock which weakens the lithosphere thereby enabling extension.

However, the source of asthenospheric melt for the RVP is still contentious. Some studies suggest the asthenospheric melt beneath the RVP arises from thermal perturbations in

the upper mantle associated with rising mantle rocks or plume head materials, while others propose melting occurs from upwelling asthenosphere due to lithospheric modulated convection (LMC) where the lithosphere is thin. Chapter 2 of this dissertation is focused on testing the hypothesis that asthenospheric melt feeding the RVP can be generated from LMC. We develop a 3D thermomechanical model of LMC beneath the RVP and the entire Malawi Rift that incorporates melt generation. We find decompression melt associated with LMC upwelling ($\approx$3 cm/yr) occurs at a maximum depth of 150 km localized beneath the RVP.

Studies of volcanic rock samples from the RVP indicate plume signatures which are enigmatic since the RVP is highly localized, unlike the large igneous provinces in the Eastern Branch of the EAR. In chapter 3, we investigate melt generation from plume-lithosphere interactions (PLI) beneath the RVP. We develop a 3D model of convection using information from seismology we call tomography-based convection (TBC) beneath the RVP. The seismic data indicate excess temperatures of $\approx 250K$ beneath the RVP suggesting the presence of a plume. We find a relatively fast upwelling ($\approx$10 cm/yr) beneath the RVP which we interpret as a rising plume. The TBC upwelling generates decompression melt at a maximum depth of $\approx$200 km beneath the RVP. Our results demonstrate that an excess heat source from may be plume materials is necessary for melt generation in the sublithospheric mantle beneath the RVP because passive asthenospheric upwelling of ambient mantle will require a higher than normal mantle potential temperatures to generate melt.

Dedication

To my wife, Elizabeth Fomenky and kids: Drake, Estella, and Daniella Njinju-Atem

Acknowledgments

I would like to express special thanks to my advisor, Dr. D. Sarah Stamps, for her guidance, mentoring, and continuous support during my time at Virginia Tech. Thanks also go to my committee members: Dr. Scott King, Dr. Ying Zhou, and Dr. Estella Atekwana for the guidance and constructive suggestions that have greatly improved my research. Dr. King suggested the name lithospheric modulated convection.

I am thankful to the faculty members of the Geosciences and Mathematics departments for the quality knowledge transferred to me. I will also like to thank the office and technical staffs for being an essential part of the Department of Geosciences at Virginia Tech. Special thanks to the EarthCube Leadership Council for granting me the opportunity to learn and practice leadership skills by electing me as an Early Career At-Large member. I am also thankful to the EarthCube Balto team for the exchange of ideas between developers and scientists in our regular meetings.

Special thanks to the Geodesy and Tectonophysics Laboratory (GTL) group for our insightful weekly update meetings during which we get recommendations and support from each other to improve our research. I am really proud of our commitment in diversity, equity and inclusion. I am also grateful to my fellow graduate students for the time spent together and for exchanging constructive ideas.

I also want to offer a special thanks to my mother, brothers, sisters and my in-laws for their support. And most importantly special thanks to my wife, and kids for their uncondi-

tional love and support.

Contents

List of Figures

List of Tables

Chapter 1

Lithosphere-Asthenosphere Interactions: Implication for Magma-Poor Rifting Processes

A modified version of this work has been published in Tectonics as:

Njinju, E. A., Atekwana, E. A., Stamps, D. S., Abdelsalam, M. G., Atekwana, E. A., Mickus, K. L., ... & Nyalugwe, V. N. (2019). Lithospheric Structure of the Malawi Rift: Implications for Magma-Poor Rifting Processes. *Tectonics*, 38(11), 3835-3853.

1.1 Abstract

Our understanding of how magma-poor rifts accommodate strain remains limited largely due to sparse geophysical observations from these rift systems. To better understand the magma-poor rifting processes, we investigate the lithosphere-asthenosphere interactions beneath the Malawi Rift, a segment of the magma-poor Western Branch of the East African Rift System. We developed a three-dimensional (3D) numerical model of edge-driven convection (EDC) beneath the Malawi Rift and surroundings where we use the lithospheric structure derived from spectral analysis of Bouguer gravity anomalies from the World Gravity Model

2012 to constrain the initial temperature structure. We assume a viscoplastic rheology for the crust governed by parameters for wet quartzite, while the rheology for the lithospheric and sublithospheric mantle are respectively governed by dislocation and diffusion creep laws of dry olivine. Our convection model indicates $\approx 3\ cm/yr$ asthenospheric upwelling beneath the thinner lithosphere. We propose that coupled extension beneath rift's isolated magmatic zones is assisted by lithospheric weakening due to melts from asthenospheric upwelling; whereas decoupled extension beneath rift's magma-poor segments is assisted by concentration of fluids possibly fed from deeper asthenospheric melt that is yet to breach the surface.

1.2 Introduction

Continental rifts are elongate, tectonically induced depressions within the Earth's continents. They are underlain by lithosphere that has been modified by extension and typically characterized by volcanism, thinning of the crust and lithospheric mantle, low seismic velocities, and elevated heat flow (Olsen, 1995; Thybo & Nielson, 2009). Numerical models for continental rift initiation highlight the importance of an actively upwelling asthenosphere followed by extensive magmatic diking that thermally weakens the lithosphere and may reduce the force required to tectonically stretch an initially thick continental lithosphere up to a factor of six (e.g., Buck, 2006; Schmeling, 2010). Numerous studies point to the important role of magma and fluids in rift initiation because tectonic stretching requires forces that are greater than is tectonically available to extend and thin the lithosphere to lead to lithospheric rupture (e.g., Buck, 2006; Stamps et al., 2010, 2014). Globally, there is ample support for magma-assisted rifting provided by the occurrence of surface magmatism associated with many rift systems such as the Eastern Branch of the East African Rift System (EARS) (Figure 1.1)(Ebinger, 2005; Kendall et al., 2005). However, numerous examples also exist worldwide where rifting is accompanied by limited exposure of volcanic rocks, such as in the Rio Grande Rift (Wilson et al., 2005) and the Malawi Rift, which is the focus of this study and represents the southern segment of the Western Branch of the EARS (e.g., Ebinger et al., 1989; Fontijn et al., 2012; Heilman et al., 2019).

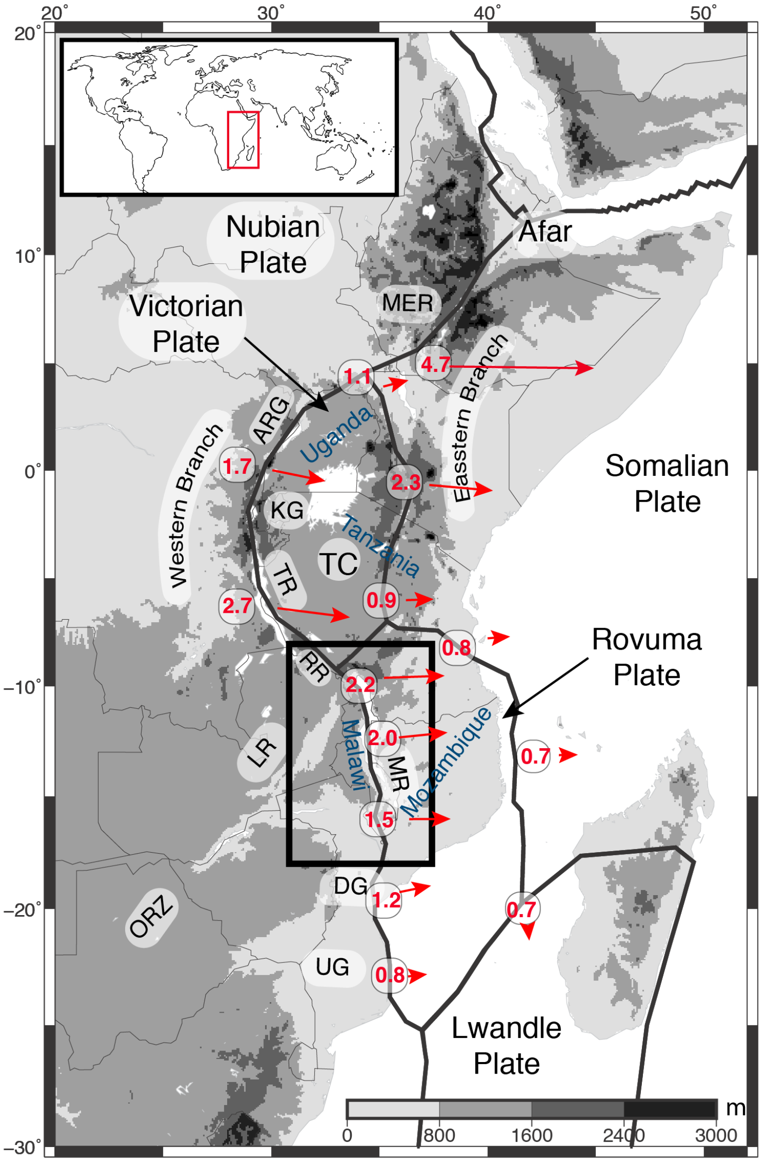

Figure 1.1: (a) Digital Elevation Model (DEM) extracted from the Global 30 arc second Elevation Data (GTOPO30) showing the East African Rift System (EARS) with the Eastern and Western branches of the EARS. MER = Main Ethiopian Rift. ARG = Albertine-Rhino Graben. KG = Kivu Graben. TR = Tanganyika Rift. TC = Tanzanian Craton. RR = Rukwa Rift. MR = Malawi Rift. LR = Luangwa Rift. DG = Dombe Graben. UG = Urema Graben. ORZ = Okavango Rift Zone. VI = Victoria Plate. RV = Rovuma Plate. LW = Lwandle Plate. The black rectangle indicates the study area shown in Figure 1.2a. Red vectors are predicted velocities representing surface motion (mm/yr) relative to the Nubian Plate from Saria et al. (2014). Black bold lines represent plate boundaries from Stamps et al. (2008). Black thin lines delineate international borders with the names of the main countries transect by the Western Branch labeled in blue colors. The inset map shows the relative location of the EARS (red rectangle) on Earth.

The EARS represents an ideal laboratory for studying magma-poor rifting because it comprises the two contrasting magmatic styles of rifting with the Eastern Branch being magma-rich and the Western Branch being magma-poor [Figure 1.1; Koptev et al., 2015, 2018 and references therein]. The Western Branch includes rift segments, such as the Malawi Rift, that are considered well-developed in terms of morphological expression, yet have only isolated zones of magmatism. Thus, our understanding of the role of magma in the development of magma-poor continental rifts remains unclear, and magma-poor rifts remain enigmatic. This is largely because there are inadequate geoscientific observations to accurately constraint the lithospheric and thermal structure beneath magma-poor continental rifts.

Geoscientific observations from different segments of the EARS suggest that pre-existing structure plays an important role in localization extension during the evolution of continental rift systems at both regional and local scales (e.g., Van Wijk, 2005; Corti et al., 2007; Katumwehe et al., 2015; Leseane et al., 2015; Kolawole et al., 2018). Pre-existing structure such as Precambrian suture and shear zones are regions of mechanically weak lithosphere and they are prone to reactivation (McConnell, 1972) by normal faulting when aligned within 30 ° of the trend and 10 ° of the plunge of the orientation of the maximum tensile stress (Morley et al., 2004). However, localization of extension along pre-existing zones of lithospheric heterogeneities might not be a satisfactory explanation for the Malawi Rift (Figures 1.2a and 1.2b). This is because the rift crosses a complex array of Precambrian orogenic belts and Paleozoic-Mesozoic Karoo-type structures (Laó-Dávila et al., 2015). Hence, there is a need for considering alternative mechanisms for localization of extension during the onset of the Malawi Rift that could be used to understand the evolution of other magma-poor continental rift systems. Such mechanism might include deep and far-sourced asthenospheric melt that has been lithospherically-channelized from an upwelling asthenosphere.

Magmatism in the Malawi Rift is limited to the Rungwe Volcanic Province (RVP) at its northern tip (Figure 1.2a). Grijalva et al. (2018) used P and S wave seismic tomography to image a low velocity zone (LVZ) beneath the RVP and the northern Malawi Rift. However, the source of this LVZ remains enigmatic. For example, although this anomaly does not extend deeper than 300 km, Grijalva et al. (2018) interpreted it to represent the flow of warm, mantle superplume upwelling from the southwest, beneath and around the thick lithosphere of the Bangweulu cratonic block, but the LVZ could also be due to asthenospheric upwelling from edge-driven convection (EDC). In contrast, thermomechanical modeling by Koptev et al. (2018) suggests the presence of a buoyant mantle plume material at the base of the lithosphere beneath the RVP and the northern Malawi Rift. The buoyant plume material is considered a southward branch of the rapidly upwelling Kenyan plume that is channelized into three mantle flows because of the presence of the thick lithosphere of the Tanzanian craton and the Bangweulu cratonic block. Thus, it is not clear if the LVZ of the RVP is manifesting upwelling of mantle material sourced from the southwest (Grijalva et al., 2018), the northeast (Koptev et al., 2018), or from upwelling in EDC induced by lithospheric thickness variations. Regardless of the source, it appears that the upwelling mantle material has influenced strain localization and resulted in magmatism only in the northern Malawi Rift. Improving our understanding of magma-poor rifting requires the investigation of the lithosphere-asthenosphere interactions beneath the rift.

In this work, we investigate the lithosphere-asthenosphere interactions beneath the Malawi Rift by simulating a three-dimensional (3-D) EDC model of asthenospheric flow induced by variations in the lithospheric thickness beneath the Malawi Rift and quantify the rate of lithospheric extension exerted by asthenospheric upwelling in order to better understand magma-poor rifting processes. The lithospheric structure is derived from two-dimensional (2-D) spectral analysis of Bouguer gravity anomalies of the World Gravity Map 2012 (WGM2012) (Njinju et al., 2019a).

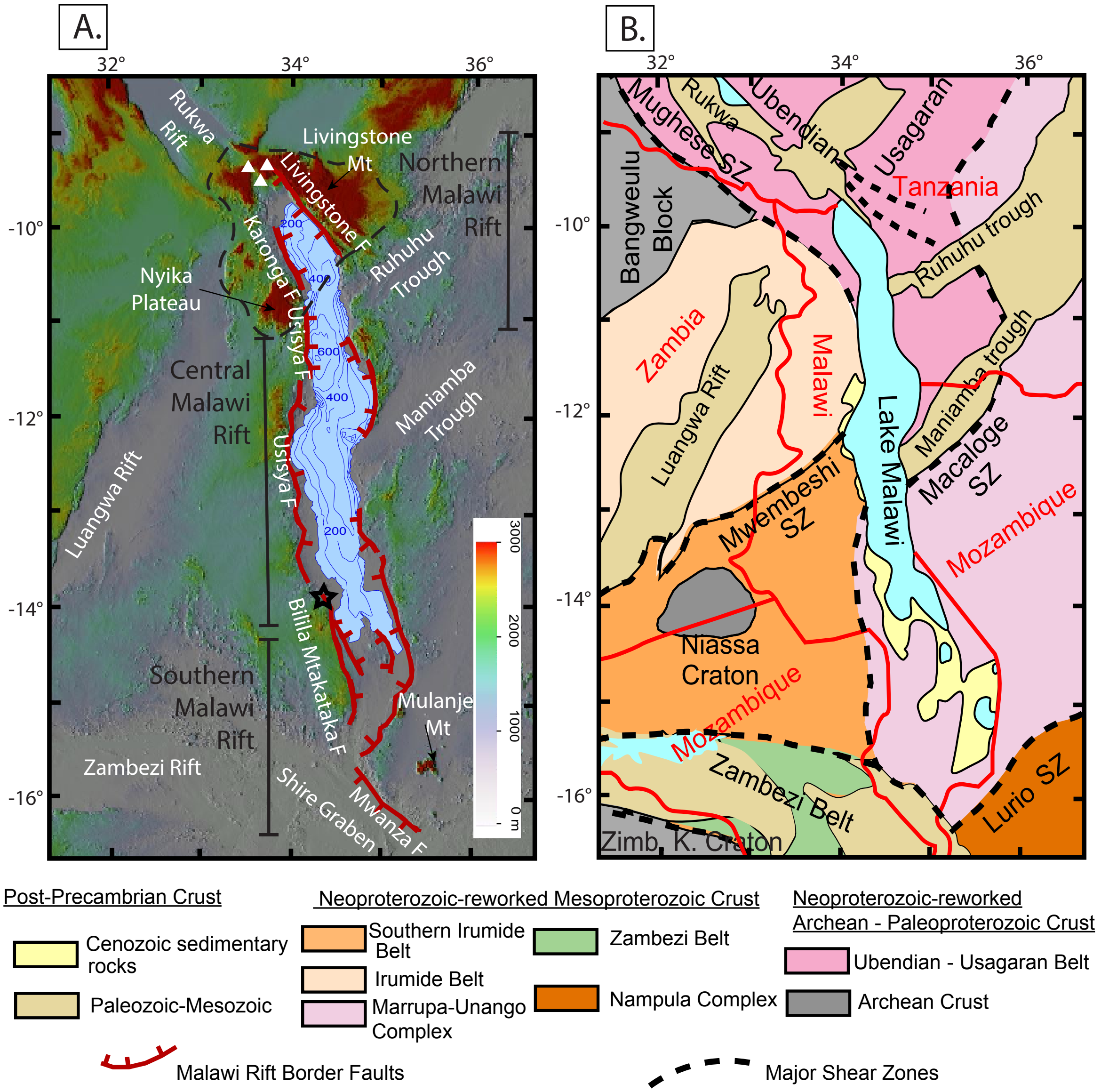

Figure 1.2: (a) Shuttle Radar Topography Mission (SRTM) Digital Elevation Model (DEM) of the Malawi Rift showing the border faults and the surrounding Paleozoic-Mesozoic Karoo rift basins corresponding to the study area (black rectangle) in Figure 1. Blue contour lines show water depth within Lake Malawi. F = Fault. Dashed black line represents uplifted region including the Rungwe Volcanic Province (white triangles), the Nyika Plateau and the Livingston Mountain. The black star represents the epicenter of the March 10, 1989 earthquake in Malawi. (b) Tectonic map showing the exposures of the Precambrian and Paleozoic-Mesozoic units around the Malawi Rift. Modified after Westerhof et al. (2008), Fritz et al. (2013) and Laó-Dávila et al. (2015). SZ = Shear Zone. Zimb. K. Craton = Zimbabwe Kalahari Craton. Red lines show country borders. The legend corresponds to Figures 2b except for the Malawi Rift border fault which is in Figure 1.2a.

1.3 The Malawi Rift

1.3.1 Tectonic Setting and Architecture of the Malawi Rift

The Malawi Rift (Figures 1.2a and 1.2b), which is the southern segment of the Western Branch of the EARS, extends for ≈900 *km* from southern Tanzania, through Malawi, to northern Mozambique. The rift is largely magma-poor except for the Pliocene-Pleistocene RVP located in northern tip of the rift (e.g., Ebinger et al., 1989; Fontijn et al., 2012; Heilman et al., 2019). From north to south, the first 550 *km* extent of the rift is occupied by Lake Malawi, which has a width ranging between 50 and 75 *km*. In the north, the rift strikes is NNW-trending and then continues with a general N-S trend before assuming a NNE-trend at its southern end (Figures 1.2a and 1.2b).

The Malawi Rift is bounded by curvilinear border faults, the most prominent of them is the ≈ 120*km* long W-dipping Livingstone border fault located at the eastern side of the nothern Malawi Rift (Figure 1.2a). The 2009 Mw 6.0 Karonga earthquake in the northern Malawi Rift is related to migration of tectonic activity from the Livingstone border fault onto the hanging wall faults (Biggs et al., 2010; Fagereng, 2013; Gaherty et al., 2019) where the earthquake reactivated pre-rift Precambrian basement structures along the hanging wall hinge zone (Kolawole et al., 2018). The ≈200 *km* long Usisya fault system dominates the central Malawi Rift [Figure 1.2a; Contreras et al., 2000; Laó-Dávila et al., 2015], whereas the ≈125 *km* long Bilila-Mtakataka Fault dominates the southern segment of the Malawi Rift (Figure 1.2a; Jackson & Blenkinsop, 1997). The southern Malawi Rift terminates against the NW-trending Shire Graben bounded by the Mwanza Fault (Figure 1.2a; Castaing, 1991).

Previous studies of the Malawi Rift observe a southward decrease in the amount of the basin's subsidence, thickness of the Cenozoic-Quaternary sedimentary rocks, and elevation of the topographic escarpments (Specht & Rosendahl, 1989; Flannery & Rosendahl, 1990; Betzler & Ring, 1995). These observations are used to suggest that the northern Malawi Rift is relatively older than its southern part and provide evidence for southward propagation of the rift and its opening in a "zipper-like" fashion from north to south (Flannery & Rosendahl, 1990; Betzler & Ring, 1995). This zipper-like N-S opening of the Malawi Rift is supported by geodetic studies, which suggest that the rift is opening at a surface velocity of 2.2 mm/yr in the north and 1.5 mm/yr in the south due to an eastward movement of the Rovuma Plate away from the Nubian Plate (Figure 1.1; i.e. Stamps et al., 2008; Saria et al., 2014). Based on ^{40}Ar/^{39}Ar radiometric dating of samples from the RVP, Ebinger et al. (1993) conclude that rifting at the northern tip of the Malawi Rift started $\approx 8.6Ma$, with volcanism continuing to the present. However, recent ^{40}Ar/^{39}Ar radiometric dating of samples from the RVP by Mesko et al. (2014) place the onset of active volcanisms at $\approx$17 Ma.

1.3.2 Pre-Rift Basement Structures of the Malawi Rift

The Malawi Rift traverses a complex array of Precambrian orogenic belts and Paleozoic-Mesozoic Karoo-type sedimentary basins (Figures 1.2a and 1.2b). Studies by Laó-Dávila et al. (2015) suggest that pre-existing lithospheric heterogeneities control a hierarchal segmentation of the Malawi Rift. The NNW-strike of the nothern Malawi Rift is parallel to the tectonic fabrics of the Paleoproterozoic Ubendian Belt (Ring et al., 2002; Laó-Dávila et al., 2015; Heilman et al., 2019). In the northern Malawi Rift, the Mughese Shear Zone and other shear zones within the Ubendian Belt control the border and intrabasinal fault development (Ebinger et al., 1987; Daly et al., 1989; Wheeler & Karson, 1989; Ring, 1994; Delvaux et al., 2012; Dawson et al., 2018; Kolawole et al., 2018; Heilman et al., 2019). In the central

Malawi Rift, particularly south of the Mwembeshi Shear Zone and the Macaloge Shear Zone, the rift is at high angle to the pre-rift Precambrian basement structure and the border faults are poorly developed [Figure 1.2b; Laó-Dávila et al., 2015]. The Mwembeshi Shear Zone represents the boundary between the Irumide Belt in the NW and the southern Irumide Belt to the SE [Figure 1.2b; Fritz et al., 2013]. The pre-Mesoproterozoic Niassa Craton is located in the southern Irumide Belt (Giacomo, 1984; Daly et al., 1989; De Waele et al., 2006; Sarafian et al., 2018). The southern Irumide Belt is sutured to the Marrupa-Unango Complex by a shear zone that is sub-parallel to the to the surface expression of the Malawi Rift [Figure 1.2b; Westerhof et al., 2008]. In the southern termination of the Malawi Rift, the Precambrian basement is comprised of the NW-trending Neoproterozoic Zambezi Belt (Hanson et al., 1994; Hargrove et al., 2003), which represents the westward continuation of the Precambrian Lurio Belt (Sacchi et al., 2000).

1.4 Previous Geophysical Studies of the Malawi Rift

A number of previous studies have been conducted to investigate the crustal and upper mantle structure beneath the Malawi Rift using controlled-source seismic (lake bottom seismometers), body and surface wave tomography, and receiver function stacking (O'Donnell et al., 2013; Reed et al., 2016; Accardo et al., 2017). O'Donnell et al. (2013) used Rayleigh wave phase velocity to invert for a 3-D shear wave velocity model and observed pronounced velocity lows beneath the northern and southern ends of the Lake Malawi, but not beneath the central portion of the lake. However, the origin of the low velocity zones is not well understood.

Reed et al. (2016) used receiver function stacking to image the 410 and 660 km discontinuity and observed a normal mantle transition zone (MTZ) beneath the entire Malawi Rift indicating the absence of any thermal anomaly due to a deep hot asthenospheric upwelling at the MTZ. However, in the central Malawi Rift, Reed et al. (2016) observed an apparently uplifted zone of 20 km within both the 410 and 660 km discontinuities, which they interpreted to be due to the presence a cold and strong cratonic lithosphere. A surface wave tomography study by Fishwick (2010) found an E-W belt of thick lithosphere ($\approx 180 - 210km$) beneath the central and southern Malawi Rift. Reed et al. (2016) interpreted the belt of thick lithosphere to represent the eastward continuation of cratonic lithosphere of the Congo and Kalahari Cratons.

Accardo et al. (2017) used lake bottom seismometers and onshore ambient noise and teleseismic Rayleigh wave phase velocities to determine the crustal and uppermost mantle structure beneath the notherm Malawi Rift and found decrease in velocities at longer periods (25-60s) consistent with the replacement of the colder higher velocity lithospheric mantle by hotter slower asthenospheric mantle. This low velocity anomaly is to the west of Lake Malawi and persists beneath the Mughese Shear Zone and Nyika plateau. Accardo et al. (2017) suggest that the presence of localized melting beneath the RVP may be due to thermal or compositional anomalies in the upper mantle, synrift or pre-rift lithospheric thinning, or a combination of both.

1.5 Methods

We simulate 3-D convection in the asthenosphere down to 500 *km* beneath the Malawi Rift due to lateral variations in lithospheric thickness using the adiabatic boundary plug-in of the open source finite element code, ASPECT (Advanced Solver for Problems in Earth's ConvecTion) (Kronbichler et al., 2012; Heister et al., 2017; Bangerth et al., 2018) to test the potential role of lithosphere-asthenosphere interactions in magma-poor rifting along the Malawi Rift. We investigate the lithosphere-asthenosphere interactions beneath the Malawi Rift by generating an EDC model. EDC is asthenospheric convection driven by small density pertubation at the base of the lithosphere from lateral temperature variations due to variations in the lithospheric thickness (King & Anderson, 1998).

The lithospheric structure beneath the Malawi Rift and surroundings based on the spectral analysis of Bouguer gravity anomalies from the World Gravity Model 2012 (Njinju et al., 2019a) range from 115 to 210 *km* (Figure 1.3). The lithosphere is generally thin beneath the entire length of the Malawi Rift. The lithosphere has an average thickness of ≈140 *km* beneath the surface expression of the Malawi Rift and is thinnest (115-130 *km*) beneath the northern and southern Malawi Rift. The central Malawi Rift is underlain by an E-W trending belt of relatively thick lithosphere that ranges from 180 to 210 *km* thick beneath the Precambrian terranes of the eastern and western flanks of the rift. We use a combination of the gravity-derived lithospheric structure (Njinju et al., 2019a), surrounded by sesimically-derived lithospheric structure [Figure 1.4a; Fishwick, 2010] to define the initial thermal structure.

We assume an initial thermal structure of the lithosphere characterized by a linear gradient from the Earth's surface (298.15 K) to the lithosphere-asthenosphere boundary (LAB) (1673.15 K) while the sublithospheric temperature increases approximately adiabatically (0.5 K/km) to the base of the model (Figure 1.5b). We investigate instantaneous mantle flow, where the initial thermal structure is used to characterize the buoyancy force.

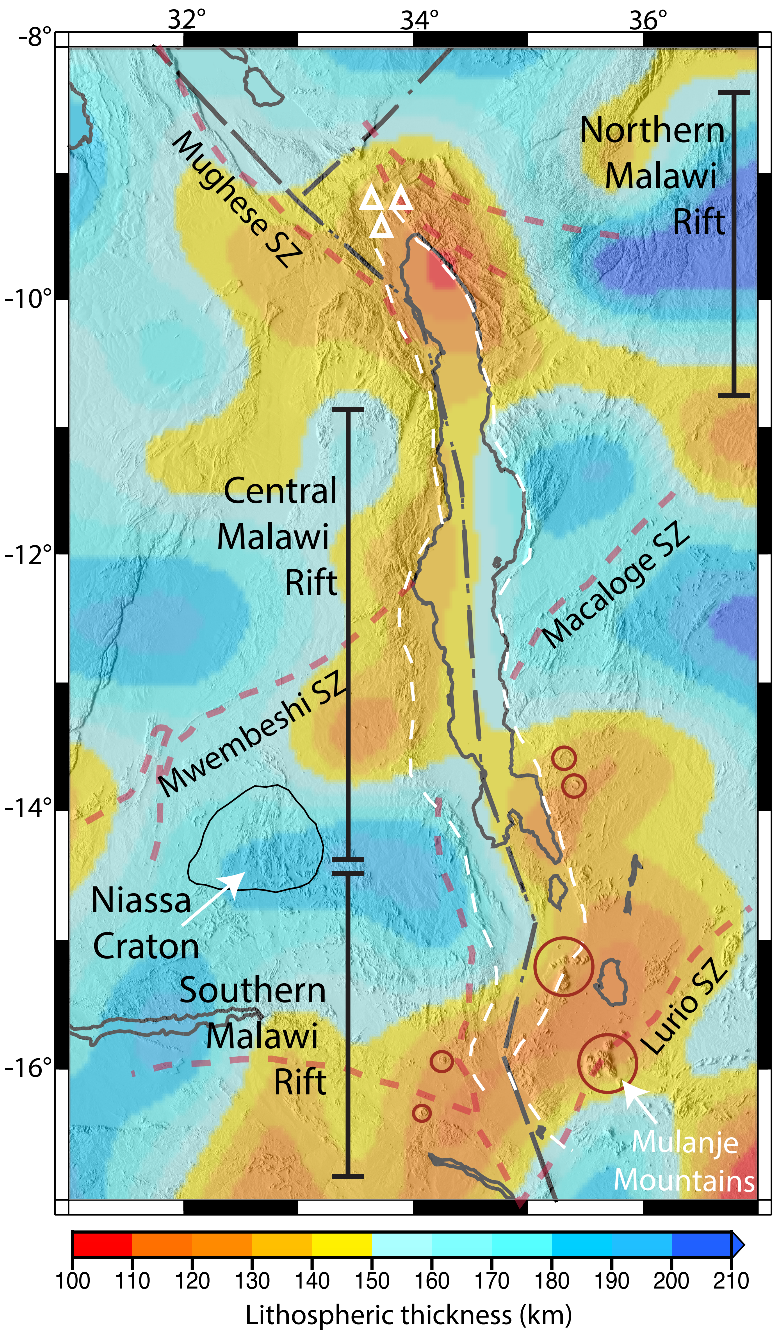

Figure 1.3: Lithospheric thickness map of the Malawi Rift and surroundings obtained from the two-dimensional (2-D) radially averaged power spectrum analysis of Bouguer gravity anomalies from the World Gravity Model 2012 (Njinju et al., 2019a). The lithospheric thickness map is draped onto SRTM-DEM (Figure 1.2a). Red dashed lines represent shear zones (SZ). Red circles represent location of Ring-Complexes observed on the SRTM-DEM. Dash-dotted black lines represent plate boundaries from Stamps et al. (2008).

We simulate the EDC model by solving for the velocity term **u** in the Stokes flow equation, which is the conservation equation for momentum (Eq. 1.1) and mass (Eq. 1.2) for an incompressible fluid.

$$-\nabla \cdot [2\eta \, \varepsilon(\mathbf{u})] + \nabla p = \rho \mathbf{g} \qquad \text{in } \Omega, \tag{1.1}$$

$$\nabla \cdot \mathbf{u} = 0 \qquad \text{in } \Omega \tag{1.2}$$

where $\varepsilon(\mathbf{u}) = \frac{1}{2}(\nabla \mathbf{u} + \nabla \mathbf{u}^T)$ is the symmetric gradient of the velocity. $\mathbf{u}$, p, η, $\mathbf{g}$ are respectively the velocity field, the pressure field, viscosity of the mantle, and the gravitational acceleration. This numerical model uses a radial Earth-like gravity model, where the unit vector of $\mathbf{g}$ points towards the center or the Earth.

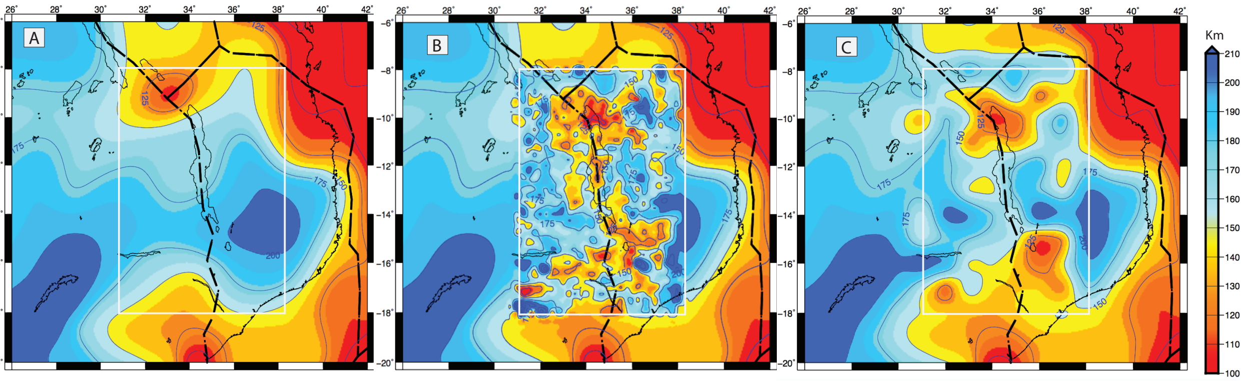

Figure 1.4: (a) Seismically-derived lithospheric thickness (Fishwick, 2010). (b) Gravity-derived lithospheric thickness (white box) surrounded by the seismic LAB, both merged at 0.5° × 0.5° interval. (c) Same as (b) but merged at 0.75° × 0.75° interval, which is our preferred lithospheric thickness model. Black lines represent plate boundaries from Stamps et al. (2008).

The buoyancy force driving mantle convection is proportional to both the density of the fluid, and the gravitational acceleration. We simplify the above equations by applying the

Boussinesq approximation, which ignores density variations except for the buoyancy term ($\rho\mathbf{g}$) where the density varies linearly with temperature (Eq. 1.3):

$$\rho = \rho(T) = \rho_0(1 - \alpha(T - T_0)) \tag{1.3}$$

ρ_0 is the reference density at reference temperature T_0 and α is the linear thermal expansion coefficient. For the earth's mantle, $\rho_0 = 3300\ kg/m^3$, and for the crust, $\rho_0 = 2700$ kg/m^3, $T_0 = 293.15K$, and $\alpha = 2.10^{-5}\ 1/K$ (Kronbichler et al., 2012; Heister et al., 2017; Bangerth et al., 2018).

The model geometry is an ellipsoidal chunk defined as 1400 km along the longitudinal axis, 1600 km along the latitudinal axis and 500 km deep (Figure 1.5a). The model domain we investigate using our main lithospheric structure model derived from gravity data is 550 × 1000 × 500 km (white box in Figure 1.4). We assume a uniform crustal thickness of 30 km and the base of the lithosphere is defined by a 1673.15 K isotherm (see below). We tested both zero velocity boundary conditions and tangential flow at the boundary of the model, where the velocity is parallel to the model boundary (see section 1.5.1).

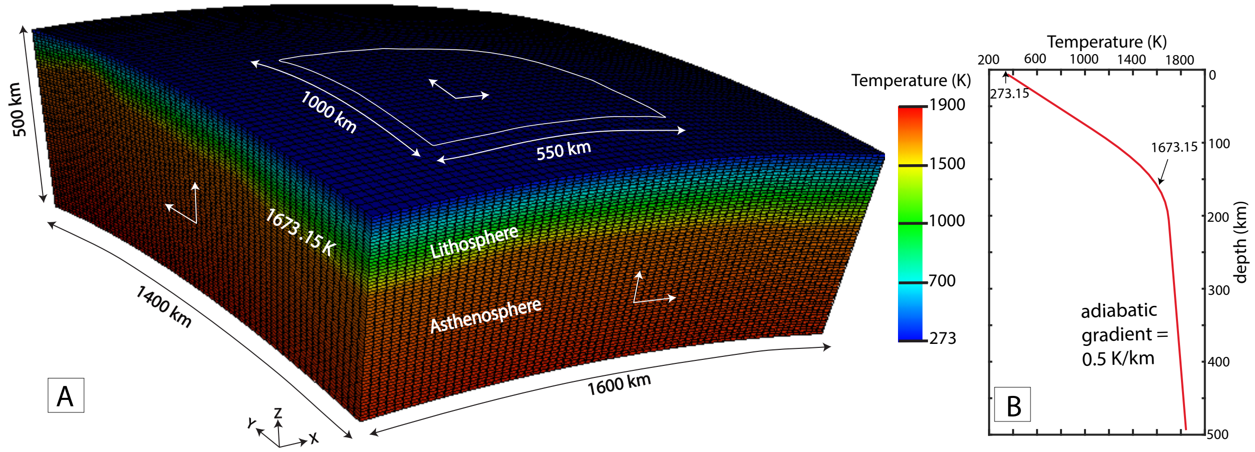

Figure 1.5: Model setup showing the model dimensions, global mesh refinement, and an initial temperature condition as the background in 3-D (a). The white box corresponds to the region with gravity derived lithospheric thickness. White arrows represent tangential boundary conditions. (b) Initial temperature profile in 2-D averaged over the entire model.

Mantle convection is strongly influenced by variations in viscosity. In this work we use a non-linear (non-Newtonian) viscosity flow law to model a realistic Earth. The crustal rheology is governed by the viscoplastic flow law of wet quartzite (Ranalli, 1995; Table 1.1). The lithospheric mantle and the sublithospheric mantle follows dislocation creep and diffusion creep flow laws respectively (Eq. 1.4; Karato & Wu, 1993; Koptev et al., 2015). Because olivine is the most abundant and also the weakest mineral in the upper mantle based on microstructural analysis of peridotite, we characterize the rheology of the upper mantle using olivine material parameters (Karato & Wu, 1993; Table 1.1).

The equation used for mantle rheology is (Bangerth et al., 2018):

$$\eta_{\text{diff, disl}} = \frac{1}{2} A^{-\frac{1}{n}} d^{\frac{m}{n}} \dot{\epsilon}^{\frac{1-n}{n}} \exp\left(\frac{E_a + pV_a}{nRT}\right) \tag{1.4}$$

where A is the prefactor, n is the stress exponent, $\dot{\epsilon}$ is the square root of the second invariant of the deviatoric strain rate tensor, d is the grain size, m is the grain size exponent, E_a is the activation energy, V_a is the activation volume, p is pressure, R is the gas constant and, T is the temperature (Table 1.1).

1.5.1 Test of edge effects due to boundary conditions

We use seismically-derived lithospheric thickness (Fishwick, 2010) to expand the surroundings spanned by the gravity-derived lithospheric thickness to assess the influence of boundary conditions. We use two different boundary conditions to test the edge effects: i.e. zero velocity boundary condition and tangential flow boundary conditions (BC). We use parameters for dry olivine to run the two EDC models and determined the residual of their flow orientations and flow magnitudes. We observe similar flow patterns and velocity magnitudes for both the zero velocity BC and the tangential flow BC at 150 km, 250 km and 350 km depths. Within the region of interest, the average vertical velocity residual is -0.02 mm/yr, 0.02 mm/yr and -0.01 mm/yr at 150 km, 250 km and 350 km, respectively. Correspondingly, the horizontal velocity residuals are 0.8 mm/yr, 7.6 mm/yr and 2.2 mm/yr in our region of interest. These results indicate the level of uncertainty in the model. These comparisons are referencing the black boxed region of the model where we are focused (Figure 1.6). Although the influence of boundary conditions is minimal, we choose the zero velocity boundary condition as our preferred model setup because there is less influence from the boundary on the interior of the model.

Table 1.1: Rheological Parameters used in the Viscosity Flow Laws

Parameter	Symbol (unit)	Crust Viscoplastic	Mantle lithosphere Dislocation creep		Sublithospheric mantle Diffusion creep	
		wet quartzite	dry olivine	wet olivine	dry olivine	wet olivine
Activation energy	E_a (J/mol)	154×10^{3}	530×10^{3}	480×10^{3}	375×10^{3}	335×10^{3}
Activation volume	V_a (m^3/mol)		18×10^{-6}	11×10^{-6}	6×10^{-6}	4×10^{-6}
Prefactor	A ($\mathrm{Pa}^{-n} m^{m} s^{-1}$)	7.65×10^{-17}	7.4×10^{-15}	2.4×10^{-14}	4.5×10^{-15}	3.0×10^{-15}
Grain size exponent	m				3.0	3.0
Stress exponent	n	2.3	3.5	3.5	1.0	1.0
Grain size	d (mm)				2.0	2.0
Angle of internal friction		20°				
Cohesion		20°				

The rheological parameters for the mantle and sublithospheric mantle are from Hirth & Kohlstedt (2003). The prefactor in Hirth & Kohlstedt (2003) (i.e. A') is derived from uniaxial strain experiments and is converted to the plane strain equivalent (i.e. A) using the following relationships: $A = \frac{3^{(n+1)/2}}{2^{1-n}} \times 10^{-6(m+n)} C_{OH}^{r} A'$, for wet olivine and; $A = \frac{3^{(n+1)/2}}{2^{1-n}} \times 10^{-6(m+n)} A'$, for dry olivine (Becker, 2006). C_{OH} is the water content in H/10^6Si, r is a constant (r = 1 for diffusion, and r = 1.2 for dislocation creep). We assume a constant $C_{OH} = 1000$. The rheological parameters for the crust are from Ranalli (1995).

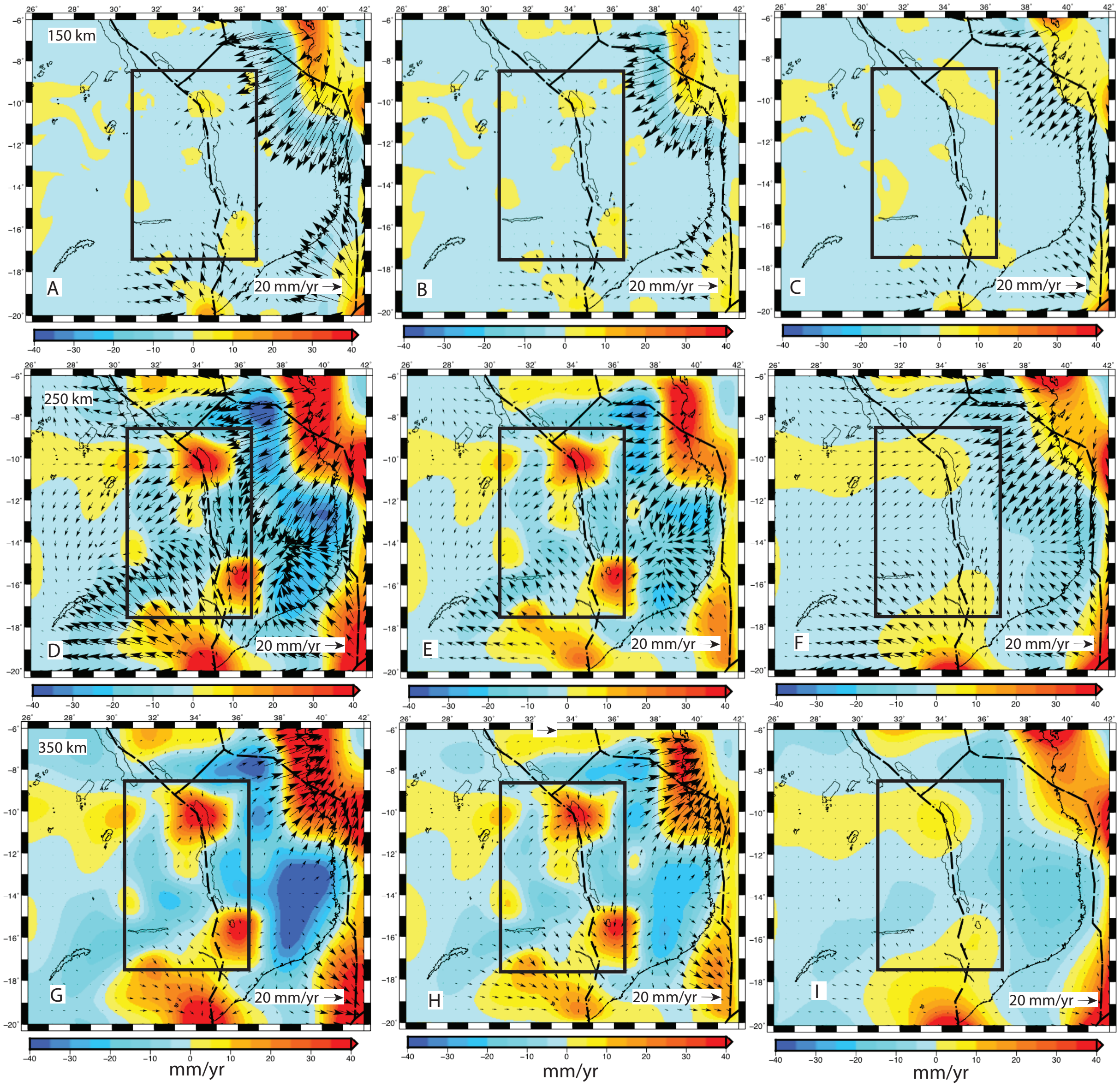

Figure 1.6: Tests of the edge effects due to boundary conditions. Vertical velocities are the background and horizontal velocities are shown as black vectors. (a) Velocity model at 150 km for tangential flow boundary conditions. (b) Velocity model at 150 km for zero boundary conditions. (c) Velocity residuals at 150 km. Same for (d), (e) and (f) at 250 km. And same for (g), (h) and (i) at 350 km. Observe the change in direction of the horizontal velocities at 350 km depths. Black box represents our velocity model based on our gravity derived lithospheric thickness, and black lines represent plate boundaries from Stamps et al. (2008).

1.5.2 Test of dry versus wet olivine as the dominant mantle minerals

We use the zero BC to calculate two EDC models, one with parameters for dry olivine and the other using parameters for wet olivine and determine their angular misfit in order to test the effect of different mantle compositions. We use two end-member sets of parameters describing dry (high viscous coupling) and wet conditions (low viscous coupling) in the upper mantle (Hirth & Kohlstedt, 2003; Table 1.1). We find similar flow patterns (angular misfit <10°). However, the velocity fields for wet olivine mantle flow models are two orders of magnitude higher than those for dry olivine as expected due to the lower viscosity associated with wet olivine parameters. Wet conditions are more appropriate in oceanic upper mantle or in continental upper mantle with subducting plates that entrain high water content materials into the mantle. However, the African continent is mainly surrounded by spreading ridges and has no subducting plates except at the northern end where there is subduction in the Mediterranean Sea region. The tectonic setting of the Malawi Rift is such that there are no plates subducting beneath the rift and the region is far from fertile oceanic lithosphere. We choose dry olivine as our preferred mantle composition for the EDC (Figure 1.7). Our preferred models are therefore models using rheological parameters for dry olivine.

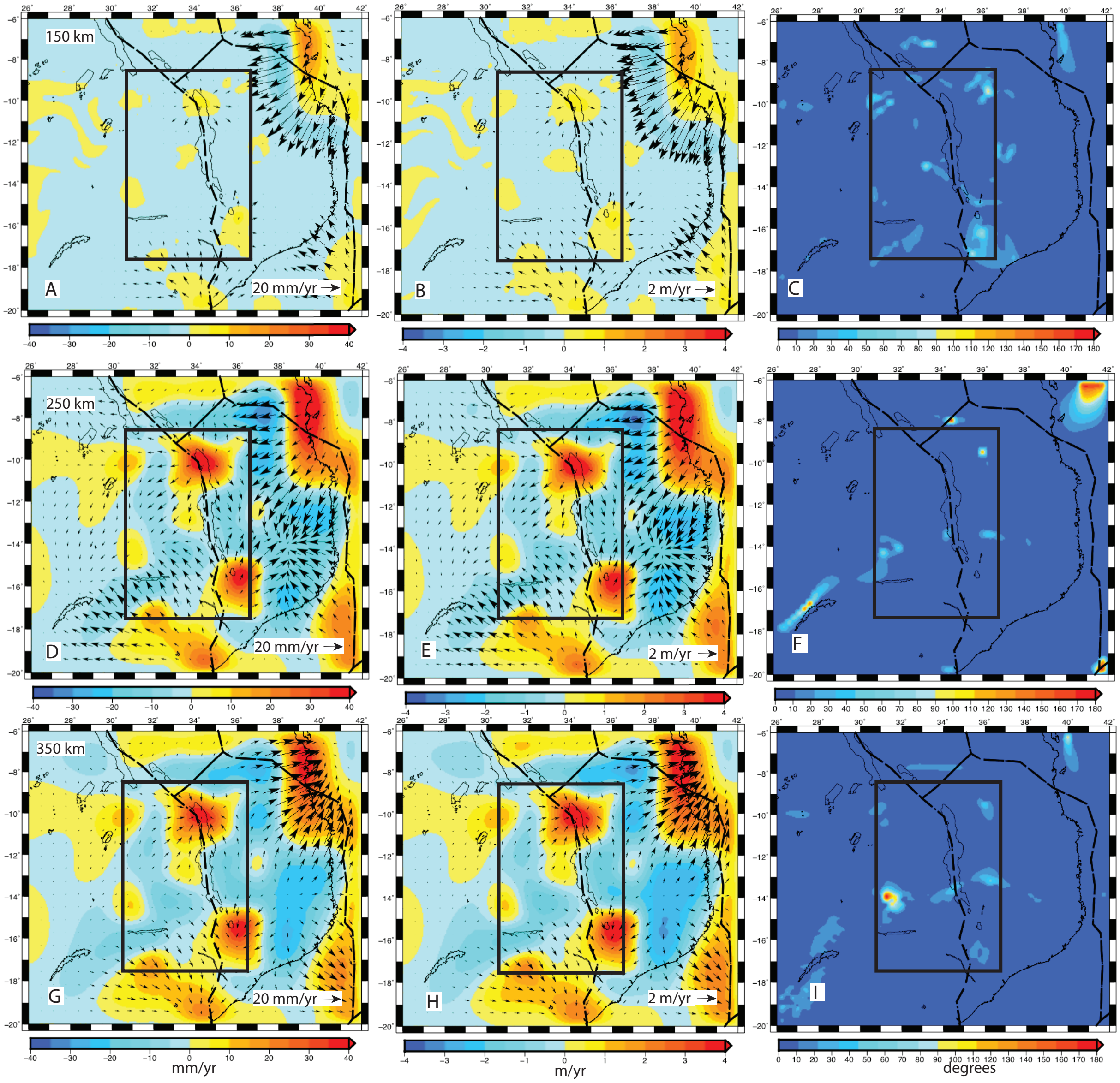

Figure 1.7: Tests of dry versus wet olivine material parameters. Vertical component of velocity is in the background with horizontal velocities shown as black vectors. (a) Velocity model at 150 *km* for dry olivine. (b) Velocity model at 150 *km* for wet olivine. (c) Angular misfit of the velocities for dry olivine and wet olivine velocity models at 150 *km*. Same for (d), (e) and (f) at 250 *km*. And same for (g), (h) and (i) at 350 *km*. Observe the change in direction of the horizontal velocities at 350 *km* depths. Black box represents our velocity model based on our gravity derived lithospheric thickness, and black lines represent plate boundaries from Stamps et al. (2008).

1.6 Results

Figures 1.8a and 1.8b show lithospheric deformation and asthenospheric flow patterns resulting from our numerical modeling of EDC. Our results indicate there may be asthenospheric upwelling (≈3 cm/yr) beneath the RVP and beneath the northern and southern Malawi Rift driven by EDC. Minor upward (≈1 cm/yr vertical velocities) and diverging (<0.5 cm/yr horizontal velocities) displacement of the lithospheric mantle at ≈150 km in the northern Malawi Rift and to the southeastern flank of the Malawi Rift (Lurio Shear Zone) is present. Deformation patterns in the lithospheric mantle are spatially consistent with modeled EDC in the asthenosphere at ≈250 km depth (Figure 1.8b), indicating the coupling of the asthenosphere to the lithosphere. Crustal velocities are negligible, which may indicate crust-mantle decoupling. Our model is used to suggest a southwestward flow of the upwelling mantle in the northern Malawi Rift towards the cratonic lithosphere of the central Malawi Rift. At deeper depths (≈350 km) there is change in the direction of horizontal mantle flow with an inward radial flow pattern beneath the zones of mantle upwelling indicating that the depth limit of the upwelling is shallower than 350 km (Figures 1.6 and 1.7).

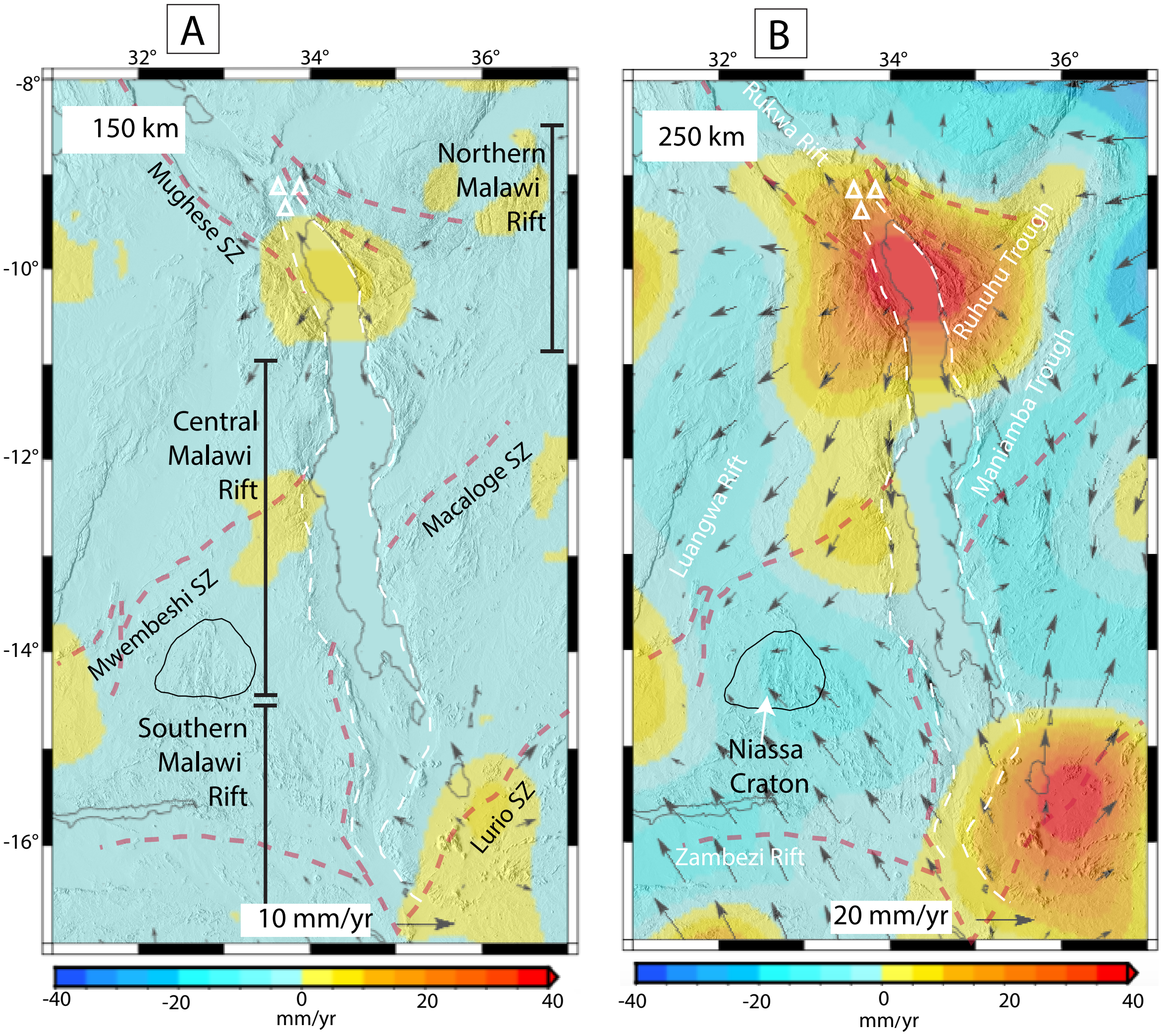

Figure 1.8: Vertical component of velocity overlain by the horizontal component of the velocity fields (black arrows) derived from the 3-D-numerical modeling of the lithospheric deformation due to sublithospheric mantle flow. (a) Deformation of the lithospheric mantle at 150 km depth. (b) Edge-driven convection of the asthenosphere at 250 km depth. The map of the vertical component of velocity is draped onto Shuttle Radar Topography Mission (SRTM) Digital Elevation Model (DEM) from which the rift outline (white dotted lines) is traced. Red dotted lines represent Shear Zones (SZ). White triangles represent the Rungwe Volcanic Province.

1.7 Discussion

We suggest that in areas of magma-poor rifting such as the Western Branch of the EARS, zones of localize crustal magmatism are characterized by coupled crust-lithospheric mantle extension, and rift segments far-field of the magma centers are characterized by decoupled crust-lithospheric mantle extension. This suggestion provides insight into the lithospheric structure of rift segments far-field of isolated magmatic centers along the Western Branch of the EARS (Figure 1.1).

We propose that the northern Malawi Rift underwent magma-assisted rifting that resulted in coupling of the extension between the crust and the lithospheric mantle. The presence of thin lithosphere (Figure 1.3) allowed asthenospheric upwelling beneath the RVP and beneath the northern and southern Malawi Rift (Figure 1.8) and this resulted in the production of asthenospheric decompression melt. In the northern Malawi Rift, melt may intrude the crust through shear zones such as the Mughese Shear Zone (Figures 1.3b and 1.9). The presence of decompression melt in the northern Malawi Rift is supported by the presence of uppermost mantle low velocity zone at depth of 68 km (O'Donnell et al., 2013). Southwestward flow of the upwelling asthenosphere from the northern Malawi Rift (Figures 1.8b and 1.9) towards the central Malawi Rift possibly led to thermal erosion of the base of the thick cratonic lithosphere, thereby enabling localization of extension in this part of the Malawi Rift. Furthermore, rifting of the thick cratonic lithosphere beneath the south-central Malawi Rift might have been additionally facilitated by asthenospheric fluids transported by the southwestward flow of the upwelling asthenosphere beneath the northern Malawi Rift. Typically, percolation of asthenospheric fuilds leads to metasomatic refertilization of the lithospheric mantle (Schutt & Lesher, 2010). Adding fluids to peridotite of the initially dry and depleted lithospheric mantle can mechanically weakening it, hence allow for localization of extension (Peslier et al., 2012). Similarly, lithospheric extension in the southern Malawi Rift might have been partially facilitated by mechanical weakening of the lithospheric mantle through metasomatic refertilization from fluids sourced from deep asthenospheric upwelling (Figure 1.8b).

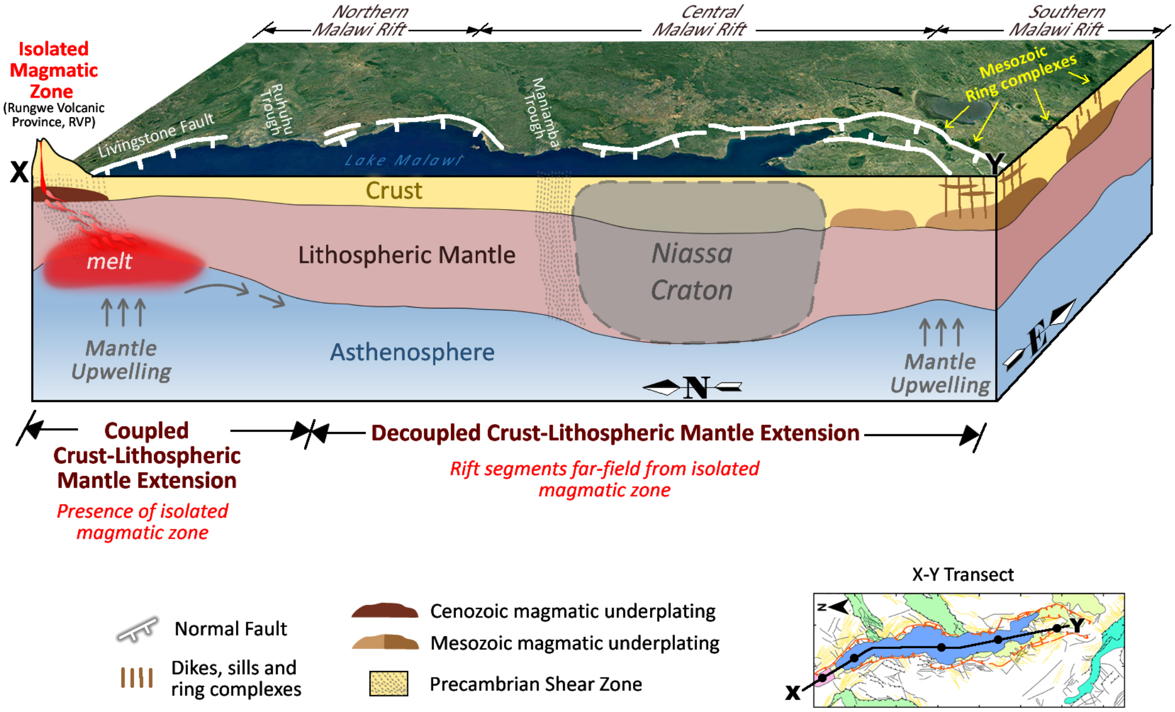

Figure 1.9: Conceptual three-dimensional (3-D) model summarizing the geodynamic and geological interpretations from this project. Thinning of the lithosphere in the northern Malawi Rift generates passive upwelling and decompression melts, which possibly migrate along Precambrian shear zones as conduits to feed the Rungwe Volcanic Province (RVP). Southward mantle facilitates strain localization in the central Malawi Rift. Thinning of the lithosphere in the southern Malawi Rift is interpreted to be pre-Cenozoic rifting, and is associated with the Mesozoic ring complexes, associated intrusions, and underplating magmatic bodies in the southern Malawi Rift region.

1.8 Conclusions

In this study, we investigate lithosphere-asthenosphere interactions beneath the Malawi Rift and surroundings by using the lithospheric structure derived from the spectral analysis and 2-D forward modeling of the WGM 2012 Bouguer gravity anomalies to constrain 3-D numerical modeling of EDC beneath the Malawi Rift. The 3-D EDC model indicates asthenospheric upwelling beneath the thin lithosphere of the northern and southern Malawi Rift with possible generation of decompression melt. We conclude that magma-assisted rifting is an important mechanism for the development of magma-poor continental rifts, particularly in isolated magmatic zones where the lithosphere is thin and there is lithospheric weakening by localized injection of asthenospheric melt. Whereas, fluids-assisted rifting, where fluids are migrating from far distance asthenospheric upwelling sources, is an important mechanism for the development of segments of the continental rifts where magmatism is apparently absent because lithospheric extension which is facilitated by metasomatic refertilization from deep asthenospheric fluids may be decoupled from the crust.

Acknowledgments

The WGM 2012 can be obtained from the International Gravimetric Bureau (BGI) free of charage. This project is supported by the NSF EarthCube Integration grant 1740627. We thank the Computational Infrastructure for Geodynamics (geodynamics.org), which is funded by the National Science Foundation under award EAR-0949446 and EAR-1550901 for supporting the development of ASPECT. We thank Editor John Geissman for handling the manuscript version and two anonymous reviewers for detailed and constructive comments.

Chapter 2

Lithospheric Control of Melt Generation Beneath the Rungwe Volcanic Province, East Africa

A modified version of this work is in revisions for publication in Journal of Geophysical Research: Solid Earth as:

Njinju, E. A., Stamps, D. S., Neumiller, K., & Gallager, J. (2020). Lithospheric Control of Melt Generation Beneath the Rungwe Volcanic Province, East Africa. *Journal of Geophysical Research: Solid Earth.* The paper is currently undergoing revisions.

2.1 Abstract

The Rungwe Volcanic Province (RVP) is a volcanic center in an anomalous region of magma-assisted rifting positioned within the magma-poor Western Branch of the East African Rift (EAR). The source of asthenospheric melt for the RVP is enigmatic, particularly since the volcanism is highly localized, unlike the Eastern Branch of the EAR. Some studies suggest the source of asthenospheric melt beneath the RVP arises from thermal perturbations in the upper mantle associated with an offshoot of the African Superplume flowing from the SW, while others propose a similar mechanism, but from the Kenyan plume diverted around the Tanzania Craton from the NE. Another possibility is decompression melting from upwelling asthenosphere due to lithospheric modulated convection (LMC) where the lithosphere is thin. We test the hypothesis that asthenospheric melt feeding the RVP can be generated from LMC. We develop a 3D thermomechanical model of LMC beneath the RVP and the entire Malawi Rift that incorporates melt generation. We assume a rigid lithosphere with laterally varying thickness and use non-Newtonian, temperature-, pressure- and porosity-dependent creep laws of anhydrous peridotite for the sublithospheric convecting mantle. We find decompression melt associated with LMC upwelling ($\approx$3 cm/yr) occurs at a maximum depth of 150 km localized beneath the RVP. We also suggest asthenospheric upwelling due to LMC entrains plume materials that do not penetrate the transition zone into the melt. Decompression melting associated with upwelling due to LMC may also provide melt sources for other continental regions of thinned lithosphere.

2.2 Introduction

Melt intrusions into the lithospheric mantle and crust during extensional tectonics play a key role in weakening the lithosphere during magma-assisting rifting. Magma-assisted continental rifting involves magmatic intrusions that are sourced from melt generated in the upper asthenosphere beneath the rift axis, which develops when mantle potential temperatures are higher than average (i.e. McKenzie & Bickle, 1988). The source of melt generation in the upper asthenosphere beneath rifts has been proposed to originate from thermal perturbations due to plumes (e.g., Burke & Dewey, 1973; Furman et al., 2006; Saunders et al., 1992) or asthenospheric upwelling in response to thinned, extended lithosphere (e.g. Nielsen &

Hopper, 2002; van Wijk et al., 2001; White & McKenzie, 1989).

The magma-poor Malawi Rift, which is the southernmost rift segment of the Western Branch of the East African Rift (EAR; Figure 2.1), provides a natural laboratory to investigate the source of asthenospheric melt. In particular, the source of sublithospheric melt for the Rungwe Volcanic Province (RVP), located in the northern region of the Malawi Rift, is contentious. Based on P and S wave seismic tomography, Grijalva et al. (2018) hypothesize deep melt beneath the RVP arises from flow of warm, mantle superplume rising from the southwest that upwells beneath and diverts around the thick lithosphere of the Bangweulu cratonic block. In contrast, thermomechanical modeling by Koptev et al. (2018) suggests that the melt beneath the RVP is sourced from the Kenyan plume that is channeled into three mantle flows by the thick lithospheric keel of the Tanzanian craton and the Bangweulu cratonic block. Alternatively, Yu et al. (2020) suggest passive mantle upwelling distinct from plume sources explains upper mantle 3D seismic velocity and radial anisotropy structures. We hypothesize that the melt beneath the RVP is, at least, partly generated from decompression melting associated with the passive upwelling model.

Here, we produce a 3D regional thermomechanical geodynamic model of passive upwelling driven by lithospheric modulated convection (LMC) beneath the RVP and the Malawi Rift using ASPECT (Advanced Solver for Problems in Earth's ConvecTion; Bangerth et al., 2018; Heister et al., 2017; Rose et al., 2017) to test the latter hypothesis. LMC is asthenospheric convection generated from temperature variations due to lateral variations in lithospheric thickness. An isotherm is assumed for the base of the lithosphere with an approximate adiabatic increase in temperature below the lithosphere. The model also takes into account rheological flow laws that allow for the generation of sublithospheric melts in a continental setting.

This study is part of the EarthCube project BALTO (Brokered Alignment of Long-Tail Observations), which is aimed at developing new, state-of-art cyberinfrastructure that enables brokered access to diverse geoscience datasets. One of the BALTO developments is a new plug-in for the community extensible NSF open-source finite element code ASPECT that permits the user to access data on the internet using web services from any remote server that uses DAP (Data Access Protocol; Gallagher et al., 2004). This study is a use-case of this BALTO cyberinfrastructure, which accesses lithospheric thickness (Fishwick et al., 2010 updated) to constrain LMC and calculate melt generation beneath the RVP and the Malawi Rift. LMC has a pattern upwelling beneath the RVP at rates of up to 3 cm/yr where lithosphere is relatively thin and produces southern asthenospheric flow along the Malawi Rift. We suggest the upwelling may entrain plume materials that do not penetrate the transition zone, which explains high ^{3}He/^{4}He detected in RVP lavas (Hilton et al., 2011). A significant percentage of asthenospheric melt from LMC occurs at depths of $\approx$130 − 155 km localized beneath the RVP, consistent with the location and maximum depth ($<$200 km) of slow P-wave velocity anomalies beneath the RVP (Yu et al., 2020). These results suggest a plume head that penetrates the transition zone is not required to explain available geochemical and geophysical observations of the Malawi Rift. The source of asthenospheric melt from LMC provides a source for shallower lithospheric intrusions of magma that weaken the lithosphere (i.e. Buck, 2006), thereby enabling magma-assisted rifting in the northern Malawi Rift. Our results indicate LMC is also a likely source of melt for volcanoes in continental regions underlain by shallow lithosphere.

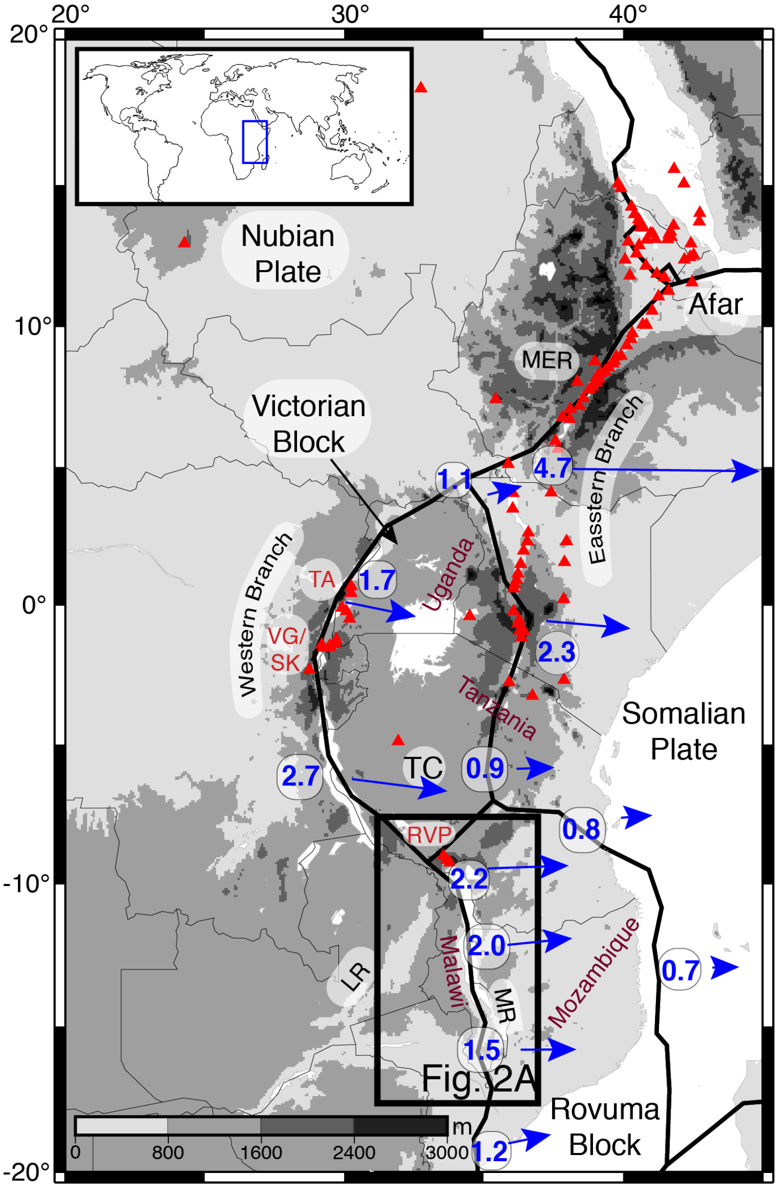

Figure 2.1: Digital Elevation Model (DEM) extracted from the Global 30 arc second Elevation Data (GTOPO30; DAAC, 2004) showing the Eastern and Western Branches of the East African Rift (EAR). The Eastern Branch of the EAR shows more volcanic centers (red triangles) than the Western Branch. MER = Main Ethiopian Rift. TC = Tanzanian Craton. MR = Malawi Rift. LR = Luangwa Rift. Red labels indicate volcanic centers in the Western Branch. TA = Toro Ankole. VG/SK = Virunga and South Kivu. RVP = Rungwe Volcanic Province. The black rectangle labeled Fig. 2A indicates the study area shown in Figure 2.2A. Blue vectors are predicted velocities representing surface motion (mm/yr) relative to the Nubian Plate from Saria et al. (2014). Black thin lines delineate international borders with the names of the main countries transect by the Western Branch labeled in brown colors. The inset map shows the relative location of part of the EAR (blue rectangle) on Earth.

2.3 Tectonic Setting

2.3.1 The Malawi Rift

The Malawi Rift, which represents the southern prolongation of the Western Branch of the EAR (Figure 2.1), is a weakly extended rift (stretching factor of 1.54; Njinju et al., 2019a) that spans 900 km from southern Tanzania, through Malawi, to northern Mozambique. The Malawi Rift (Figure 2.2A) is characterized by asymmetric half grabens bounded by curvilinear border faults with records of deep seismicity suggesting that the border faults extend to the base of the crust (Craig et al., 2011; Ebinger et al., 2019). Indeed, geophysical studies reveal a thick crust ($\approx 38-45$ km; Borrego et al., 2018; Njinju et al., 2019a) and a relatively strong and thick lithosphere beneath the central Malawi Rift ($\approx 115-210$ km; Fishwick, 2010 updated; Njinju et al., 2019a). Geodetic studies, suggest that the rift is opening at a surface velocity of 2.2 mm/yr in the north and 1.5 mm/yr in the south due to an eastward movement of the Rovuma Plate away from the Nubian Plate (Figure 2.1; i.e. Stamps et al., 2008; Saria et al., 2014). The rift is largely magma-poor with volcanism limited to the Pliocene-Pleistocene RVP located in the northern tip of the rift (e.g. Furman, 2006; Fontijn et al., 2012). It is possible that magmatism beneath the RVP contributes to the relatively fast spreading rate of the northern segment of the Malawi Rift.

2.3.2 The Rungwe Volcanic Province

The RVP is the southernmost volcanic region in the Western Branch of the EAR (Figure 2.1), which lies at the northern tip of the Malawi Rift at the intersection of the Rukwa Rift and Usangu Rift, and covers approximately 1500 km^2 (Figure 2.2B; Ebinger et al., 1989, 1997; Fontijn et al., 2012). The RVP comprises three large active volcanoes (Ngozi, Rungwe and Kyejo; Figure 2.2B) in addition to more than 100 cones and domes (Fontijn et al., 2010; Harkin, 1960). The RVP lies at the nexus of three major border fault systems including the Livingstone fault of the Malawi Rift, Lupa fault of the Rukwa Rift, and the Usangu border faults, all of which have been active in Miocene-Recent times (Figures 2.2B; Fotijn et al., 2012).

The relationship between the tectonic structures in the region and magmatism remains controversial (Mesko et al., 2014; Roberts et al., 2012). Ebinger et al. (1989, 1993) suggest that volcanism in the RVP was synchronous with initial faulting and that local deflections in the state-of-stress might result from plate bending under the load of the volcanoes. Radiometric studies of samples from the RVP using $^{40}\mathrm{Ar}/^{39}\mathrm{Ar}$ dating techniques suggest that magmatism in the RVP started by 19 Ma (Mesko et al., 2014; 2020) and possibly as early as 25 Ma (Roberts et al., 2012). Although the onset of rifting in the Malawi and Rukwa Rifts is poorly known, Ebinger et al. (1993) used $^{40}\mathrm{Ar}/^{39}\mathrm{Ar}$ radiometric dating of samples from the RVP to suggest that faulting along the Livingstone border fault in the northern Malawi Rift started $\approx$8.6 Ma. Moreover, U-Pb zircon ages of sediments from Lake Rukwa suggest reactivation and renewed subsidence in the Rukwa Rift at 8.7 Ma (Hilbert-Wolf et al., 2017). The ages of the RVP suggest that volcanism may predate the estimated onset of faulting along the Livingstone border fault and reactivation of the Rukwa Rift. Indeed, geophysical studies provide evidence that is consistent with thermal weakening of the lithosphere (with associated magmatism) preceding rift-related fault development (Grijalva et al., 2018; Koptev et al., 2018; Yu et al., 2020).

The source of the magma beneath the RVP still remains enigmatic. Studies by Grijalva et al. (2018) and Koptev et al. (2018) suggest the presence of a mantle plume beneath the RVP that generates melt. This hypothesis is supported by geochemical evidence from RVP lavas showing elevated mantle potential temperatures (Rooney et al., 2012) and elevated ^{3}He/^{4}He isotopic ratios (Hilton et al., 2011). However, Yu et al. (2020) suggest that the melt beneath the RVP arises from decompression melting in response to passive upwelling associated with lithospheric stretching based on relatively shallow low seismic velocity anomalies that are disconnected from seismic anomalies below the transition zone. Our study tests the latter hypothesis.

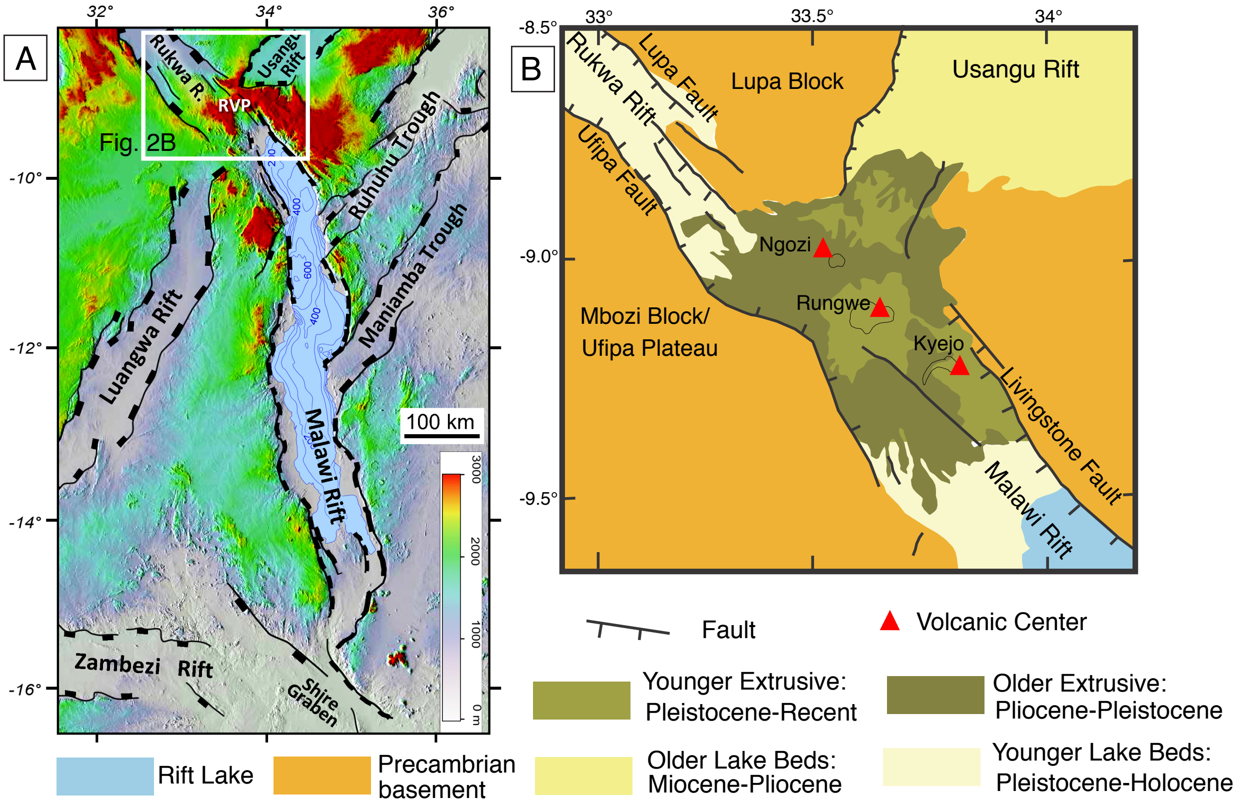

Figure 2.2: (A) Shuttle Radar Topography Mission (SRTM) Digital Elevation Model (DEM; Farr et al., 2007) of the Malawi Rift showing the border faults and the surrounding Paleozoic-Mesozoic Karoo rift basins corresponding to the study area (black rectangle) in Figure 2.1. Blue contour lines show water depth within Lake Malawi. The white box labeled Fig. 2B in Figure 2.2A shows the location of Figures 2.2B. RVP = Rungwe Volcanic Province. (B) The geological map of the RVP and the surrounding Precambrian basement. Modified after Fotijn et al. (2012). The legend is referencing Figure 2.2B.

2.4 Methods

We simulate time-dependent LMC that incorporates melt generation in the asthenosphere and transition zone in a 3D domain using the finite element code ASPECT (Bangerth et al., 2018; Heister et al., 2017; Rose et al., 2017) to test the potential role of LMC in asthenospheric melt generation beneath the RVP and the Malawi Rift. Recent studies demonstrate the capabilities of modeling melt generation and magma dynamics in ASPECT (Dannberg et al., 2019; Dannberg & Heister, 2016), however this is the first study that uses present-day lithospheric structure as input to model melt generation associated with LMC.

2.4.1 3D Lithospheric Modulated Convection Modeling

Governing Equations

We generate LMC beneath the Malawi Rift by solving for the velocity term **u** in the Stokes flow equation, which is the conservation equation for momentum (Eq. 2.1) and mass (Eq. 2.2) for an incompressible fluid:

$$-\nabla \cdot [2\eta \, \varepsilon(\mathbf{u})] + \nabla p = \rho \mathbf{g} \qquad \text{in } \Omega, \tag{2.1}$$

$$\nabla \cdot \mathbf{u} = 0 \qquad \text{in } \Omega \tag{2.2}$$

where $\varepsilon(\mathbf{u})$ is the strain rate which is the symmetric gradient of the velocity. p, η, ρ, $\mathbf{g}$ are respectively the dynamic pressure field, viscosity, density, and the gravitational acceleration. We assume an incompressibility condition for the mass conservation equation (Eq. 2.2) so that changes in density (e.g., due to pressure and temperature) are negligible. In order to model melt generation, we also simulate changes in temperature caused by heat transfer in the model by solving the energy conservation equation (Eq. 2.3). We apply the extended Boussinesq approximation that includes shear heating, adiabatic heating, and latent heat of melting in the heating model (Christensen & Yuen, 1985):

$$\begin{aligned} \rho_0 C_p \left(\frac{\partial T}{\partial t} + \mathbf{u} \cdot \nabla T \right) - \nabla \cdot k \nabla T = {} & 2\eta [\varepsilon(\mathbf{u}) : \varepsilon(\mathbf{u})] \\ & + \alpha T \left(\mathbf{u} \cdot \nabla p \right) \\ & + \rho_0 T \Delta S \left(\frac{\partial F}{\partial t} + \mathbf{u} \cdot \nabla F \right) \qquad \text{in } \Omega, \end{aligned} \tag{2.3}$$

We assume phase-independent parameterizations for the specific heat c_p and thermal expansivity , and thermal equilibrium in the entire model. k is the thermal conductivity. Based on previous studies, we assume an average crustal thermal conductivity of $k = 2.5\ W.m^{-1}.K^{-1}$ (Njinju et al., 2019b). For the lithospheric mantle, we assume an average thermal conductivity of 3.5 $W.m^{-1}.K^{-1}$ (Burov, 2011; Koptev et al., 2018) and a thermal conductivity of 4.7 $W.m^{-1}.K^{-1}$ for the sublithospheric mantle (Clauser & Huenges, 1995; Dannberg & Heister, 2016). The latent heat consumed during melting is proportional to changes in the melt fraction F and the entropy change S. The latent heat of melting is incorporated, with an entropy change of ΔS = -300 $J.kg^{-1}.K^{-1}$ (Dannberg & Heister, 2016). The buoyancy force driving mantle convection is proportional to both the density of the fluid and the gravitational acceleration. Although we assume incompressible flow for the mass conservation equation (Eq. 2.2), the density in the buoyancy term varies with both temperature and pressure:

$$\rho = \rho(T, p) = \rho_0 [1 - \alpha(T - T_0)].e^{\beta(p - p_0)} \tag{2.4}$$

where β is the compressibility coefficient, ρ_0 is the reference density at reference temperature T_0 and reference pressure p_0. We normalize the pressure to a surface pressure of $p_0 = 10^5\ Pa$ (Yang et al., 2018). For the Earth's mantle, $\rho_0 = 3300\ kg/m^3$, $T_0 = 293\ K$, $\alpha = 3 \times 10^{-5}$ K^{-1}, $c_p = 1250\ J.kg^{-1}.K^{-1}$, and $\beta = 4.2 \times 10^{-12}\ Pa^{-1}$.

Model Setup

Our model domain has dimensions of 550 × 1000 × 660 km along latitude, longitude, and depth, respectively, for a spherical chunk geometry (Figure 2.3B). However, our regions of interest beneath the RVP and the entire Malawi Rift are distant from the model boundaries so that boundary effects are limited. Based on previous tests of edge-effects on the interior of the model due to different velocity boundary conditions (free slip versus zero velocity; Njinju et al. 2019a); we set the velocities at all the sides of the model to zero which exerts minimal edge-effects on the model interior from the boundaries of the model. We refine the entire model domain to a global mesh refinement of 6 such that each element is $\approx 8 \times 15 \times 10\ km$ with 17.5 million unknowns computed on 120 cores. The model is comprised of a lithosphere and an underlying mantle that extends to 660 km depth, which includes the transition zone.

The lithospheric structure is read from the BALTO site by the BALTO-ASPECT plugin using the web services provided by the BALTO broker. The lithosphere is part of the updated lithospheric structure model of Fishwick (2010) mapped into the 3D domain for the Malawi Rift and surroundings (Figure 2.3A). The lithosphere is thinnest beneath the RVP at the northern tip of the Malawi Rift ($\approx$100 km) and also beneath the southern rift segment ($\approx$100-125 km). The lithosphere is thickest beneath the central segment of the Malawi Rift ($\approx$175-200 km). The lithospheric structure produces lateral variations in temperature and pressure such that relatively thin lithosphere has hotter geothermal gradients and lower overburden pressure than the thicker lithosphere, which is relatively colder and exerts a higher lithostatic pressure. The temperature and pressure variations due to variations in the lithospheric thickness lead to lateral density perturbations in the asthenosphere and transition zone that drive LMC (Eq. 2.4).

The initial temperature structure (Figure 2.3B) includes an approximation of a conductive geotherm for the lithosphere with a linear temperature gradient from the surface ($T_0 = 293\ K$) to the base of the lithosphere, which is an isothermal boundary defined by the mantle potential temperature T_p (Figure 2.5). The mantle potential temperature, T_p is the temperature that the mantle would have at the surface if ascended along an adiabat without melting (McKenzie & Bickle, 1988). The T_p in the RVP from eruptions occurring in the past 10 Ma ranges from 1420-1450 °C (1693 - 1723 K) based on the geochemical observations of Rooney et al. (2012). We test a range of T_p (1693, 1703, 1713, 1723 K) and find that $T_p = 1723\ K$ produces a geotherm hot enough to generate melt (Figure S1; see supporting information for details). Below the lithosphere, the temperature increases approximately adiabatically (0.4 K/km) to the base of the model (Figure 2.5). For the Earth's mantle where $\alpha = 3 \times 10^{-5}\ K^{-1}$, $C_p = 1250\ J.kg^{-1}.K^{-1}$, and $g = 9.81\ m.s^{-2}$, the adiabatic gradient beneath the RVP is given by:

$$\frac{\partial T}{\partial z} = \frac{\alpha g T_p}{C_p} \approx 0.4\ K/km \tag{2.5}$$

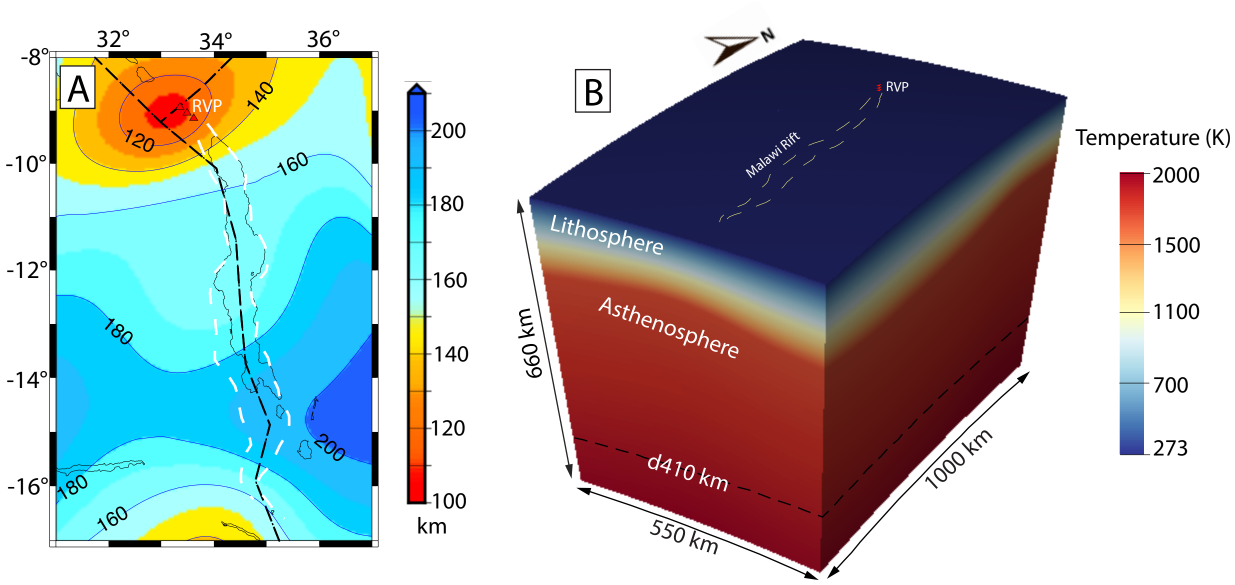

Figure 2.3: (A) Lithospheric thickness map of the Malawi Rift and surroundings, updated from Fishwick (2010) which we use as input in this study. The blue contours show lines of equal lithospheric thickness at 20 *km* intervals. Black dotted lines represent plate boundaries from Stamps et al. (2008). White dotted lines indicates the outline of the Malawi Rift traced from the Shuttle Radar Topography Mission (SRTM) Digital Elevation Model (DEM) (Figure 2.2A; Farr et al., 2007). (B) Numerical model setup showing the model dimensions and the initial temperature condition as the background in 3D. Yellow dotted lines shows the outline of the Malawi Rift. RVP = Rungwe Volcanic Province.

Rheology

Mantle convection is highly dependent on the viscosity. Since we are interested in LMC in the asthenosphere and transition zone, we impose a strong, uniform viscosity of 10^{23} $Pa.s$ for the lithosphere (Figures 2.4A and 2.4B). For the asthenosphere, we use non-Newtonian, temperature-, pressure- and porosity-dependent creep laws of anhydrous peridotite. Unlike the viscosity model of Keller et al. (2013), which is given by the application of an exponential melt-weakening factor to a constant background mantle viscosity of 10^{22} $Pa.s$, we assume the background viscosity of the sublithospheric mantle is governed by composite rheology for dry olivine material parameters (Jadamec & Billen, 2010; Rajaonarison et al., 2020). The composite rheology (comp) is the harmonic average of the viscosity from dislocation-creep (η_{disl}) and diffusion-creep (η_{diff}) flow laws of dry olivine and is given by:

$$\eta_{\text{diff, disl}} = \frac{1}{2} A^{-\frac{1}{n}} d^{\frac{m}{n}} \dot{\epsilon}^{\frac{1-n}{n}} \exp\left(\frac{E_a + pV_a}{nRT}\right) \tag{2.6}$$

$$\eta_{\text{comp}} = \frac{\eta_{\text{diff}} . \eta_{\text{disl}}}{\eta_{\text{diff}} + \eta_{\text{disl}}} \tag{2.7}$$

where A is the prefactor, n is the stress exponent, $\dot{\epsilon}$ is the square root of the second invariant of the deviatoric strain rate tensor, d is the grain size, m is the grain size exponent, E_a is the activation energy, V_a is the activation volume, p is pressure, R is the gas constant and, T is the temperature . The values for the parameters A, n, m, E_a and V_a are obtained from experimental studies of dry olivine (Hirth & Kolhstedt, 2003; Table 2.1). The viscosity of the sublithospheric mantle ($\eta_{\text{sublith-mantle}}$) with porosity dependence is given by:

$$\eta_{\text{sublith-mantle}} = \eta_{\text{comp}} . e^{-\alpha_\Phi \Phi} \tag{2.8}$$

where the exponential melt-weakening factor is experimental constrained to $25 \leq \alpha_\Phi \leq 30$ (Mei et al., 2002). We use the average value of $\alpha_\Phi = 27.5$. The porosity Φ is the ratio of the volume of pore spaces between the olivine grains of peridotite to the bulk volume of the peridotite constituent of the asthenosphere. The material properties for each layer (lithosphere and sublithospheric mantle) are tracked through compositional fields with the asthenosphere and transition zone further divided into two compositional fields called "porosity" and "peridotite". The porosity in the model is tracked through the compositional field "porosity". The viscosity at each quadrature point is calculated from the harmonic average of the compositional fields weighted by the volume fraction of each composition at the same location (Figures 2.4A and 2.4B; Rajaonarison et al., 2020).

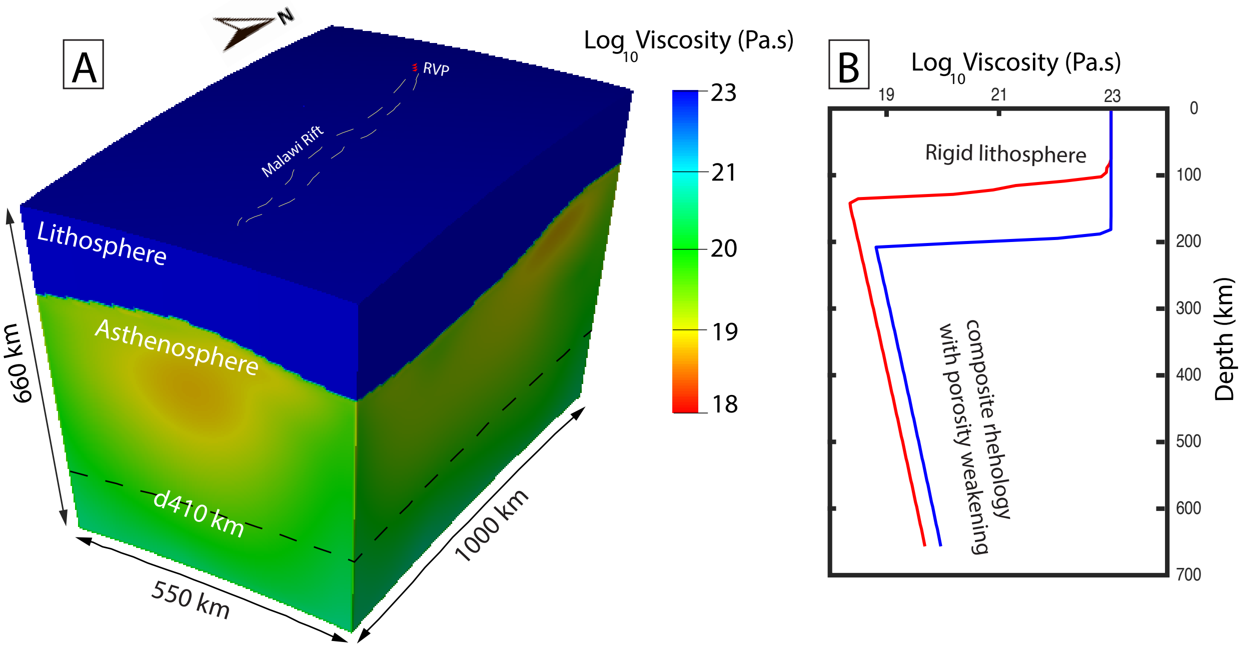

Figure 2.4: (A) Three-dimensional representation of the initial viscosity field. Yellow dotted lines show the outline of the Malawi Rift. RVP = Rungwe Volcanic Province. (B) One-dimensional initial viscosity depth profiles for a lithospheric thickness of 100 km (red) and 200 km (blue).

Setting the velocities at the bottom boundary to zero approximates the effect of the high viscosity jump across the transition zone on slowing mantle flow velocities (410 – 660 km; Ballmer et al., 2007; Rajaonarison et al., 2020). The temperature boundary conditions at all boundaries are fixed so that the net heat flux at the boundaries is zero following Rajaonarison et al. (2020).

Table 2.1: Rheological Parameters for Dry Olivine Used in the Viscosity Flow Law of the Sublithospheric Mantle

Parameter	Symbol	Dislocation creep	Diffusion creep	Unit
Activation energy	Ea	530 x 10^3	375 x 10^3	J/mol
Activation volume	Va	18 x 10^{-6}	6 x 10^{-6}	m^3/mol
Grain size	d	-	10 x 10^{-3}	m
Grain size exponent	m	-	3	-
Stress exponent	n	3.5	1.0	-
Prefactor	A	7.4 x 10^{-15}	4.5 x 10^{-15}	$Pa^{-n}m^{m}s^{-1}$

The rheological parameters for the sublithospheric mantle are from Hirth & Kohlstedt (2003). The prefactor in Hirth & Kohlstedt (2003) (i.e. A') is derived from uniaxial strain experiments and is converted to the plane strain equivalent (i.e. A) using the following relationships: $A = \frac{3^{(n+1)/2}}{2^{1-n}} \times 10^{-6(m+n)} A'$, for dry olivine (Becker, 2006).

2.4.2 Partial Melting

For efficient modeling of melt generation in the asthenosphere, we model melting of anhydrous peridotite according to Katz et al. (2003), which is valid for shallow upper mantle melting beneath continental lithosphere. Partial melting in the asthenosphere is highly dependent on the mantle potential temperature, T_p (Figure 2.5; McKenzie & Bickle, 1988), and will occur if the T_p is such that adiabatically ascending mantle intersects the solidus (Figure 2.5). The derived melt fraction $F(p,T)$ depends on the lithostatic pressure p (Pa) and temperature T (K) and is given by:

$$F(p,T) = \left(\frac{T - T_{\text{solidus}}}{T_{\text{liquidus}} - T_{\text{solidus}}}\right)^{1.5}, T_{\text{solidus}} \leq T \leq T_{\text{liquidus}} \tag{2.9}$$

where the mantle solidus temperature T_{solidus} and liquidus temperature T_{liquidus} are respectively given by:

$$T_{\text{solidus}} = A_1 + A_2 p + A_3 p^2 \tag{2.10}$$

$$T_{\text{liquidus}} = B_1 + B_2 p + B_3 p^2 \tag{2.11}$$

where $A_1 = 1085.7\ K$, $A_2 = 1.329 \times 10^{-7}\ K/Pa$, $A_3 = -5.1 \times 10^{-18} K/Pa^2$,
$\mathrm{B}_1 = 1475.0\ K$, $B_2 = 8.0 \times 10^{-8}\ K/Pa$, and $B_3 = -3.2 \times 10^{-18} K/Pa^2$.

Partial melting in the asthenosphere is also highly dependent on the lithospheric thickness. This is because a thick lithosphere serves as a mechanical barrier to adiabatic ascent of hot mantle materials. The thickness of the melt zone and the maximum extent of partial melting are limited by the lithospheric thickness (e.g., McKenzie & O'Nions, 1995). We test the sensitivity of melt generation to lithospheric thickness variations in our model by conducting simulations with varied lithospheric thickness (+10 km and -10 km) based on the model of Fishwick (2010, updated). We find that when we increase the lithospheric thickness by 10 km (increase of mechanical barrier to adiabatic ascent of hot mantle materials) no melt is generated due to LMC. However, when we reduce the lithospheric thickness by 10 km (reduction of mechanical barrier), an unrealistically high melt fraction (≈12 % melt) is generated from LMC beneath the RVP. This test also serves as a validation of the lithospheric thickness model by Fishwick (2010), which when used as an input in our model; we obtain a more realistic melt fraction (≈1.5 % melt) from LMC (see section 2.5.2). We simulated convection for 20 Ma to ensure that steady state is achieved. The melt that reaches the base of the lithosphere may refreeze, accumulate in a deep or shallow magma reservoirs, inject into the lithosphere as dikes, or erupt to create new crust, however the fate of the melt in the lithosphere is beyond the scope of this study.

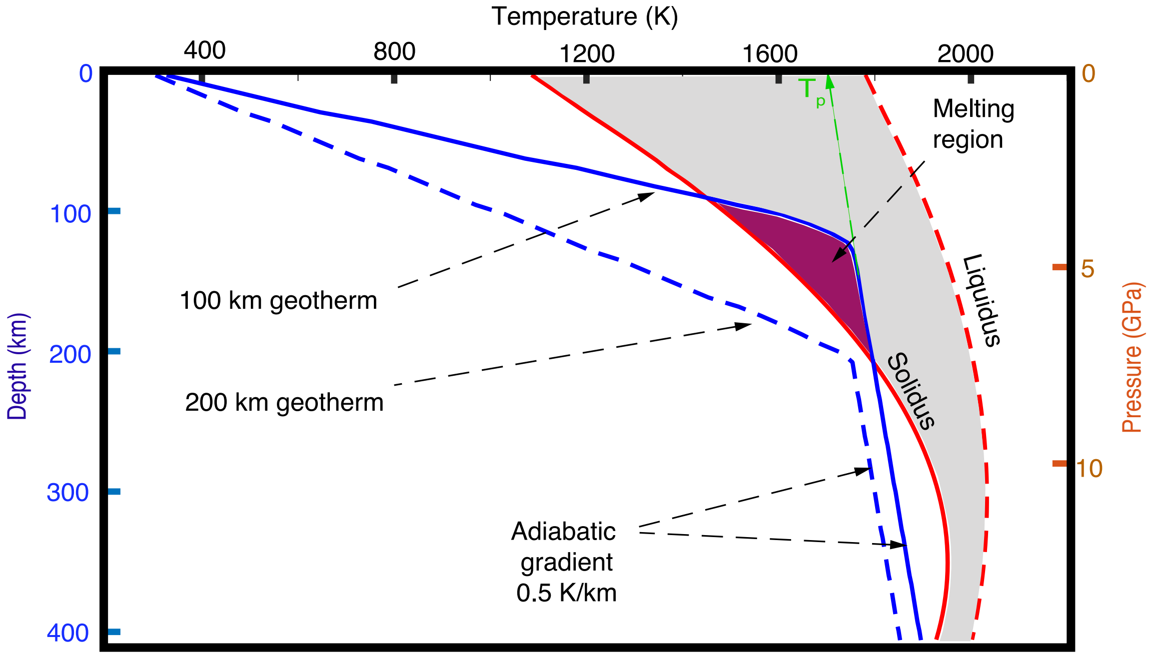

Figure 2.5: A combined plot of temperature-depth profiles (blue solid lines for a 100 km thick lithosphere and blue-dashed lines for a 200 km thick lithosphere) and a pressure-temperature phase diagram depicting shallow melting of anhydrous peridotite parameterized from Katz et al. (2003). The red solid line represents the solidus (0 % melt) and the red-dashed line represents the liquidus (100 % melt). The solidus and liquidus are plotted from Eq. 3.10 and Eq. 3.11 respectively. T_p represents the mantle potential temperature.

2.5 Results

2.5.1 Lithospheric Modulated Convection

In our simulation, LMC develops spontaneously from our initial thermal conditions and forms where there is a transition in lithospheric thickness from relatively thick to thin (see Figure 2.3A). Figures 2.6A and 2.6B show flow patterns at 17 Ma (time during which the flow is steady-state; see section 2.5.2) resulting from our numerical modeling of LMC at

150 km and 250 km depth slices, respectively. Asthenospheric upwelling occurs beneath thin lithosphere, while downwelling occurs beneath relatively thick lithosphere. Our results indicate asthenospheric upwelling beneath the RVP driven by LMC. At 150 km depth (Figure 2.6A), asthenospheric upwelling (≈1 cm/yr) with a diverging (≈2 cm/yr) horizontal flow occurs only beneath the RVP where the lithosphere is thin (≈100-120 km). At 250 km depth (Figure 2.6B), the asthenospheric upwelling beneath the RVP is faster (≈3 cm/yr). Another zone of weaker upwelling (≈0.5 cm/yr) occurs beneath the southern end of the Malawi Rift where the lithosphere is ≈160 km thick compared to the thicker lithosphere (≈180 km) in the central part of the rift. Our model suggests a southward flow of the upwelling mantle beneath the RVP towards the thick lithosphere in the central part of the Malawi Rift where the asthenospheric flow is characterized by downwelling (Figure 2.6B). The lithosphere, which is made rigid in the model, is not deforming.

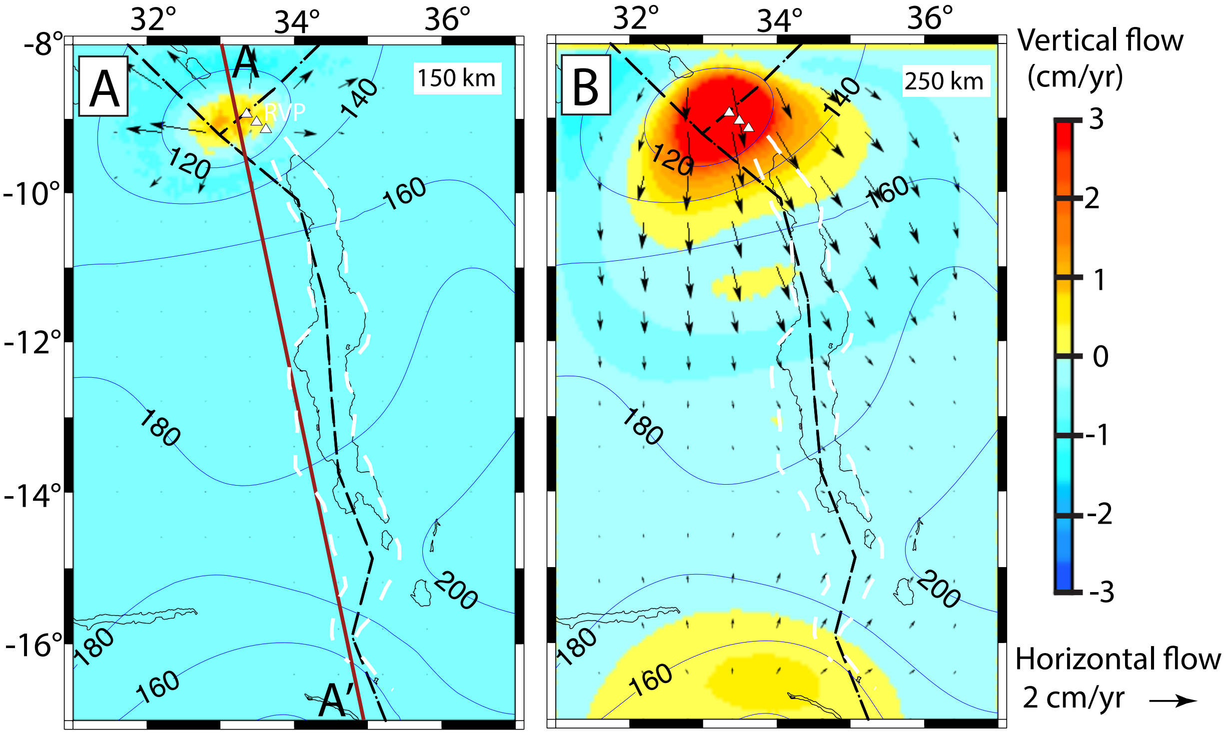

Figure 2.6: Depth slices showing lithospheric modulated convection beneath the RVP and the Malawi Rift at (A) 150 *km* and (B) 250 *km* depth at 17 *Ma*. The vertical flow (background color) is overlain by the horizontal flow field (black arrows). White dotted lines indicates the outline of the Malawi Rift traced from the Shuttle Radar Topography Mission (SRTM) Digital Elevation Model (DEM; Farr et al., 2007; Figure 2.2A). White triangles represent the RVP. Black dotted lines delineate plate boundaries from Stamps et al. (2008). Blue contours show lines of equal lithospheric thickness at 20 *km* intervals from Fishwick (2010, updated). Brown profile AA' in Figure 2.6A is the profile location for Figure 2.8.

2.5.2 Melt Generation

The time evolution of our melting model (Figure 2.7) reveals two stages of melting. The first stage, which we call the transient or unsteady melting state, occurs in the first 2 *Ma* of the model evolution beneath the RVP. The instantaneous (0 *Ma*) decompression melt (≈8.5 % melt) is not due to LMC; rather the melt arises from the initial conditions, which includes relatively thin lithosphere beneath the RVP and a high mantle potential temperature (1723 *K*; Rooney et al., 2012). Heat transfer due to LMC controls the duration of melting in the model. During this early stage in our convection model, the initial LMC is unstable and advects most of the heat to the overlying lithosphere. Moreover, there is additional heat loss due to the endothermic melting process such that the asthenosphere experiences a net heat loss. Since the asthenosphere progressively cools, melting sustained by intrinsic density variations decreases rapidly and ceases by 2 Ma (Ballmer et al., 2007). As the model evolves, LMC attains steady-state and asthenospheric upwelling convects hotter mantle materials from the lower part of the asthenosphere and transition zone to shallower sublithospheric depths. This convection leads to the second stage of decompression melting that arises from LMC where the melt fraction increases rapidly from 0 to < 1.5 % between 12-16 Ma and saturates to 1.5 % melt above 17 Ma (Figure 2.7).

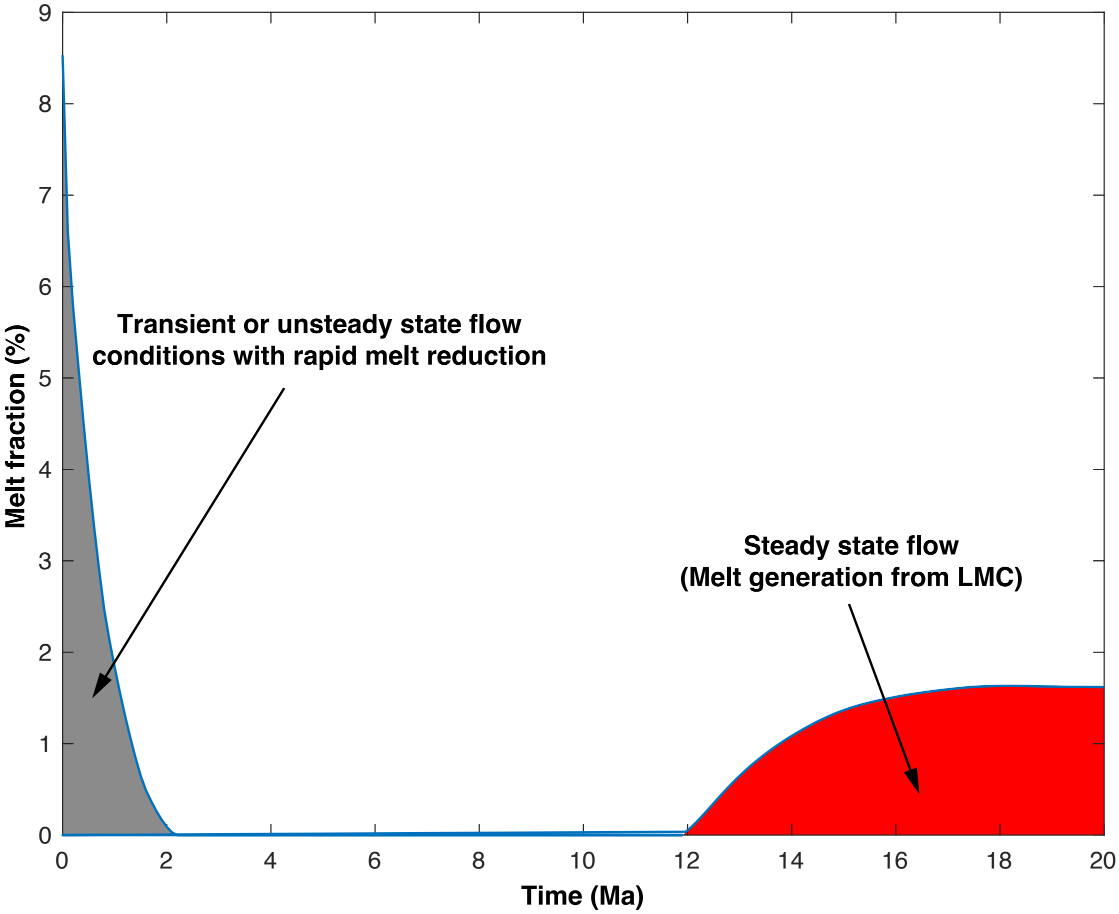

Figure 2.7: A plot of melt fraction versus time showing the evolution of melt in the model. The gray color (0 – 2 Ma) represents when lithospheric modulated convection (LMC) is unstable and the initial decompression melt (≈8.5 %) generated from the initial temperature conditions decreases rapidly and ceases at 2 Ma. The red color (12 – 20 Ma) corresponds to melt generation due to LMC, during which steady-state LMC produces strong upwelling that entrains deep, hot asthenospheric and transition zone materials to shallow, sublithospheric depths.

Figures 2.8A, 2.8B and 2.8C show time-variable LMC and melt generation for the melting parameterization of peridotite (Katz et al., 2003) across the RVP and the long axis of the Malawi Rift (profile AA' defined in Figure 2.6A). The velocity fields show a similar mantle flow pattern at 10 Ma (Figure 2.8A), 17 Ma (Figure 2.8B), and 20 Ma (Figure 2.8C) with upwelling focused beneath the thin lithosphere of the RVP. The similar flow patterns from

10 – 20 Ma suggest that LMC is stable between 10 and 20 Ma. At 10 Ma (Figure 2.7A), melt has yet to generate because the LMC has not evolved enough to entrain deep, hot asthenospheric and transition zone materials to shallow sublithospheric depths. At 17 and 20 Ma (Figures 2.8B and 2.8C, respectively), upwelling from LMC has had enough time to transport deeper mantle materials to shallower depths, raising the sublithospheric geotherm above the mantle solidus temperature that leads to decompression melting of up to 1.5 % melt fractions.

Depth slices of the melt model at 17 Ma (Figures 2.8A, 2.8B, 2.8C and 2.8D) indicate that melt generation due to LMC is restricted to depths of $\approx$ 130–155 km beneath the RVP where the lithospheric thickness is $<$120 km. The maximum melt fraction occurs at the center of the melting region ($\approx$ 145 km) with melt fractions reaching $\approx$1.5 % (Figure 2.8C). Numerical modeling of asthenospheric melt generation beneath the Baikal Rift, which is a relatively magma-poor rift similar to the Malawi Rift, produces similar results of 1 - 2 % melt fractions (Yang et al., 2018).

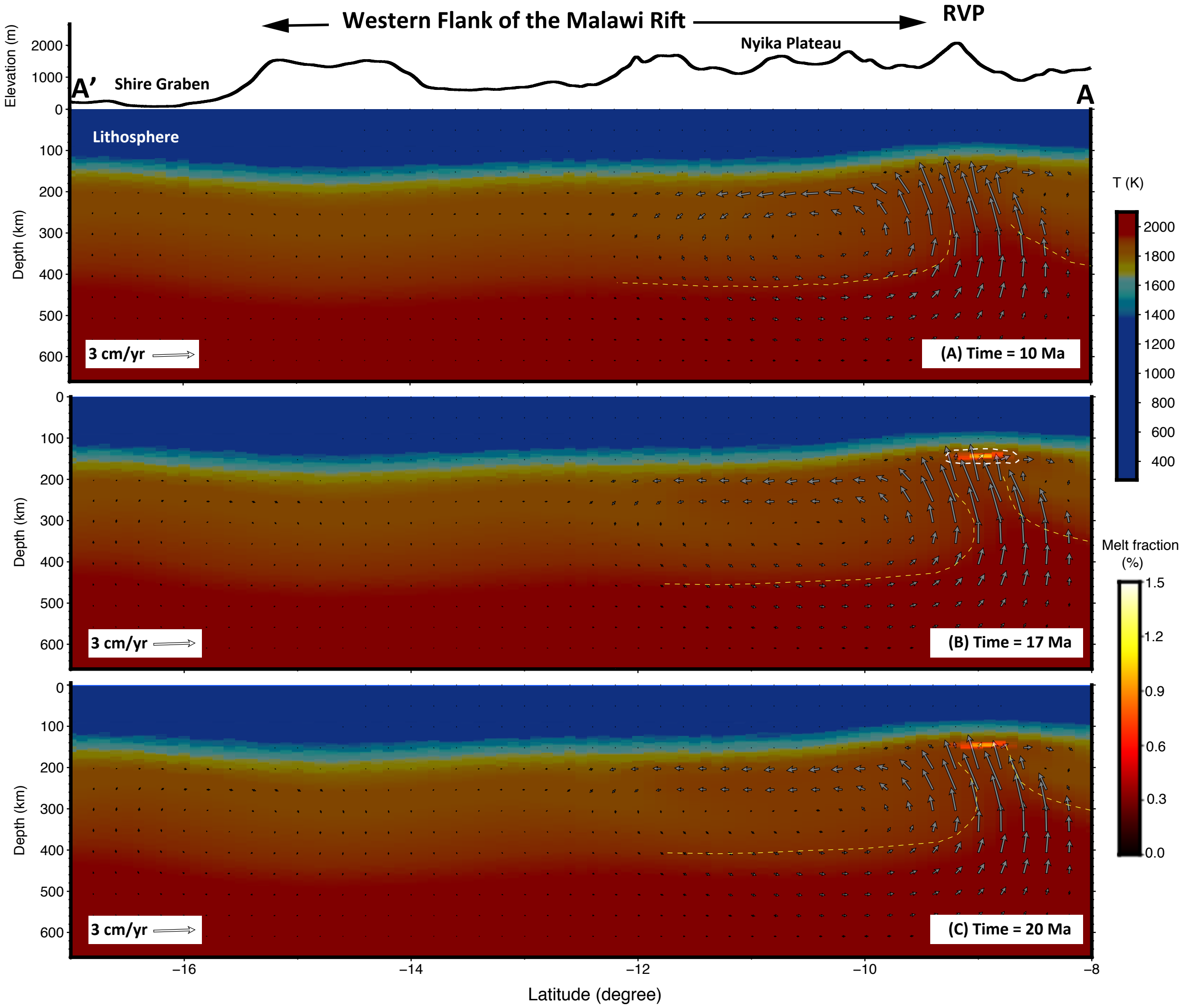

Figure 2.8: Profile showing time-dependent lithospheric modulated convection (LMC) across the Rungwe Volcanic Province (RVP) and the Malawi Rift (profile AA'; Figure 2.6A). (A) Time = 10 *Ma*. (B) Time = 17 *Ma*. (C) Time = 20 *Ma*. Note the similarity in the structure of the mantle flow indicating steady-state LMC from 10-20 *Ma*. We include the yellow dotted lines to help visualize entrainment of deep, hot asthenospheric and transition zone mantle rising to shallower depths beneath the lithosphere.

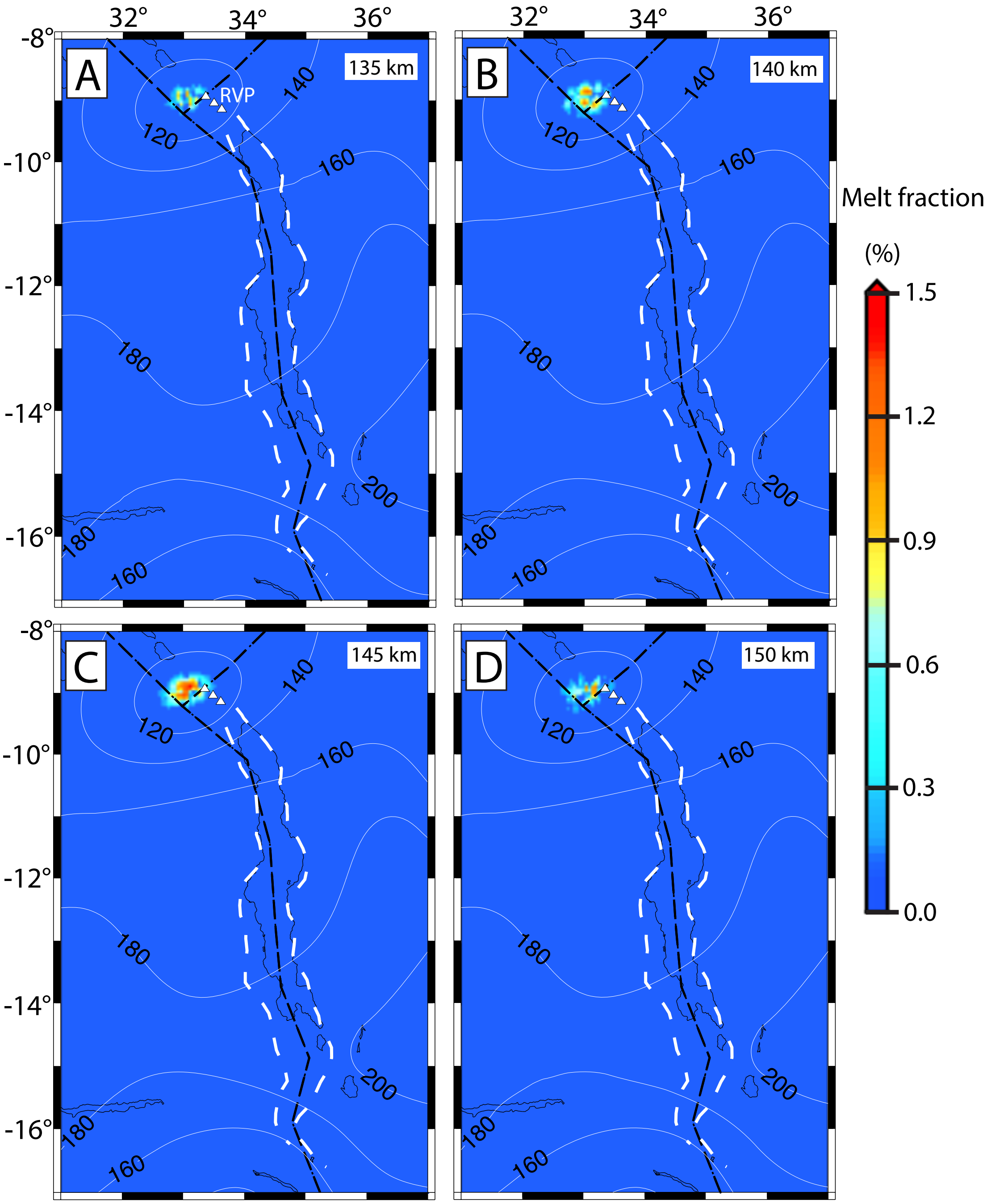

Figure 2.9: Depth slices showing melt fractions beneath the RVP and the Malawi Rift at (A) 135 *km*, (B) 140 *km*, (C) 145 *km*, and (D) 150 *km* depth at 17 *Ma*. White dotted lines indicate the outline of the Malawi Rift traced from the Shuttle Radar Topography Mission (SRTM) Digital Elevation Model (DEM; Farr et al., 2007; Figure 2.2A). White triangles represent the RVP. Black dotted lines delineate plate boundaries from Stamps et al. (2008). White contours show lines of equal lithospheric thickness at 20 *km* intervals from Fishwick (2010, updated).

2.6 Discussion

2.6.1 Sources of Deep Melt Beneath the Rungwe Volcanic Province

The most prominent features in our model are the isolated region of asthenospheric upwelling and localized decompression melting due to LMC beneath the RVP at depths of $\approx$ 130–155 km. The cross-section of the region of maximum melt generation is roughly elliptical (Figure 2.8C) with an area of $\approx$ 4000 km^2. Given that the melting region is roughly conic in shape, the volume of generated melt is $\approx$ 33,000 km^3. The RVP covers an area of $\approx$ 1500 km^2 (Fotijn et al., 2012) with a maximum elevation of $\approx$ 2.5 km (Figure 2.8A). The volume of volcanic rocks covering the RVP is, therefore, generally $<$ 3750 km^3. Thus, the ratio of intrusive versus eruptive melt volume for the RVP is $\approx$ 9:1, which is within the range of intracontinental volcanic fields that is estimated to vary between 4:1 and 10:1 (Crisp, 1984).

The melting region is spatially consistent with a pronounced low velocity anomaly (LVA) beneath the RVP imaged from P-wave anisotropic tomography using data recorded by seismic stations of the Seismic Array for African Rift Initiation experiment (Yu et al., 2020). Yu et al. (2020) found the LVA is mostly constrained to the upper mantle above 200 km depth and has no observable connection with the underlying deeper mantle. This result suggests that the LVA beneath the RVP may be a consequence of partial melts generated from LMC rather than superplume material that rises from the southwest, passes through the transition zone, and impinges the Bangweulu Craton lithosphere where it is then diverted eastward as proposed by Grijalva et al. (2018).

However, a geochemical study of lava and tephra samples from the RVP by Hilton et al. (2011) shows significantly elevated values of helium isotope ratios (^{3}He/^{4}He) of 15 RA (RA = air ^{3}He/^{4}He) which far exceeds typical upper mantle values. The high ^{3}He/^{4}He ratios associated with the RVP could be sourced from the primordial mantle in the core-mantle boundary brought to the surface by upwelling mantle plumes (Courtillot et al., 2003). Such plume-like ^{3}He/^{4}He ratios, suggest that a mantle plume contributes to the magmatism beneath the RVP. Upwelling beneath the RVP from LMC likely entrains plume materials that do not penetrate the transition zone and are unresolved by the P-wave tomographic study of Yu et al. (2020). The high mantle potential temperature (1723 K; Rooney et al., 2012) beneath the RVP is also consistent with hot plume materials being entrained into shallow asthenospheric mantle by LMC.

2.6.2 Implications for Incipient Rifting

The most prominent features in our model are the isolated region of asthenospheric upwelling and localized Our numerical model of LMC reveals an isolated upwelling beneath the RVP where the lithosphere is thin. This upwelling beneath the RVP results in the production of asthenospheric decompression melt at depths of $\approx 130 - 155$ km which is supported by the presence of LVA beneath the RVP that is mostly constrained to the upper mantle above 200 km depth (Yu et al., 2020). The asthenospheric melt may pond beneath the lithosphere and, subsequently, be injected into the mantle lithosphere and crust through preexisting lithospheric structures (Njinju et al., 2019a). Indeed, Accardo et al. (2020) used local measurements of Rayleigh-wave phase velocities to invert for shear wave velocities and clearly observed low velocities (<4.3 km/s) beneath the RVP at crust and upper-mantle depths that are consistent with the presence of injected magma. The injection of magma into the lithosphere is an important factor in the process of continental rift initiation since magma can greatly reduce the strength of thick lithosphere and facilitates rifting (Bastow et al., 2011; Buck, 2006; Kendall et al., 2005; Kendall Lithgow-Bertelloni, 2016). Recent seismic tomography models developed for the RVP and the northern Malawi Rift indicate that the lithosphere beneath the Malawi Rift may have been weakened prior to rifting (Accardo et al., 2020; Grijalva et al., 2018; Yu et al., 2020). Southward flow of the upwelling asthenosphere beneath the RVP (Figure 2.6B) towards the Malawi Rift possibly leads to thermal erosion of the base of the lithosphere, thereby enabling localization of extension in the Malawi Rift (Njinju et al., 2019a).

2.7 Conclusions

In this study, we develop a 3D thermomechanical model of LMC beneath the RVP and the Malawi Rift that incorporates melt generation. We assume a rigid lithosphere, while for the asthenosphere we use non-Newtonian, temperature-, pressure- and porosity-dependent creep laws of anhydrous peridotite. Our LMC simulation is characterized by an isolated asthenospheric upwelling beneath the RVP, which generates a significant percentage of decompression melt. Our results suggest that the asthenospheric upwelling due to LMC beneath the RVP provides a source of deep melt for these volcanoes. We also suggest LMC entrains deeper plume materials, thus explaining high ^{3}He/^{4}He values in the volcanic materials of the RVP and elevated mantle potential temperatures. We, therefore, conclude that asthenospheric upwelling due to LMC beneath the RVP provides an important source of deep melt for the region without necessitating the presence of a plume head penetrating the transition zone. LMC is therefore a likely source of melt for volcanoes in continental regions underlain by shallow lithosphere.

Acknowledgments

This project is supported by the NSF EarthCube Integration grant 1740627. Most of the figures in this paper were generated with Generic Mapping Tools V5.4.2 (Wessel et al., 2013). We also created some of the figures with VISIT v2.9 developed by the Lawrence Livermore National Laboratory. The lithospheric thickness file can be accessed from the Hyrax server through the URL http://balto.opendap.org/opendap/lithosphere_thickness/. We thank the Computational Infrastructure for Geodynamics for supporting the development of ASPECT, which is funded by National Science Foundation Awards EAR-0949446 and EAR-1550901.

Chapter 3

Plume-Lithosphere Interactions and Melt Generation Beneath the Rungwe Volcanic Province, East Africa

A modified version of this work is in preparation for submission to Geophysical Research Letters as:

Njinju, E. A., Stamps, D. S., Rajaonarison, T. , Neumiller, K., & Gallager, J., E. Atekwana (2020). Plume-Lithosphere Interactions and Melt Generation Beneath the Rungwe Volcanic Province, East Africa. *Geophysical Research Letters.*

3.1 Abstract

The Rungwe Volcanic Province (RVP) is an isolated volcanic center in the southern part of the Western Branch of the East African Rift (EAR). Studies of rock samples from the RVP indicate plume signatures, which are enigmatic, since the volcanism is highly localized, unlike the Eastern Branch of the EAR. We test the hypothesis that the melt beneath the RVP is generated from a plume. We investigate melt generation from plume-lithosphere interactions

(PLI) beneath the RVP by using seismic constraints of lithospheric and sublithospheric structures to develop a 3D thermomechanical model of tomography-based convection (TBC) and melt generation beneath the RVP using the finite element mantle convection code ASPECT. We assume a rigid lithosphere with its base defined by the mantle potential temperature (T_p) and use non-Newtonian porosity-dependent creep laws of anhydrous peridotite for the sublithospheric mantle. The seismic constraints indicate excess temperatures of $\approx$ $250K$ in the sublithospheric mantle beneath the RVP suggesting the presence of a plume. We find decompression melt ($\approx$0.25 %) associated with mantle upwelling ($\approx$10 cm/yr) occurs at a maximum depth of $\approx$200 km beneath the RVP. Our results demonstrate that an excess heat source from may be plume materials is necessary for melt generation in the sublithospheric mantle beneath the RVP because passive asthenospheric upwelling of ambient mantle will require a higher than normal T_p to generate melt.

3.2 Introduction

Plume-lithosphere interactions (PLI) play an important role in the tectonic evolution of the lithosphere by controlling the location and form of continental magmatism. The impact of a plume head beneath the lithosphere generally results in intense melting of plume materials, producing large igneous provinces (LIPs; White & McKenzie, 1989) such as in the Eastern Branch of the EAR (Figure 3.1A) (Ayalew & Gibson, 2009). However, the Western Branch of the EAR (Figure 3.1A) is characterized by limited and sparse magmatism and the melt source is contentious. In particular, geochemical studies of past eruptions of the Rungwe Volcanic Province (RVP; Figure 3.1A), which is the southernmost volcanic center in the Western Branch, indicate plume signatures. The plume signatures of the RVP remain enigmatic, mainly because the volcanism is highly localized, unlike the LIPs in the Eastern Branch (Figure 3.1A). These plume signatures includes elevated T_p (≈1420-1450 °C; Rooney et al., 2012) and high ^{3}He/^{4}He (Hilton et al., 2011).

The RVP lies at the triple junction formed by the Rukwa Rift, Usangu Rift, and the Malawi Rift within the Ubendian-Usagaran mobile belts that circumvent the thick lithosphere of the Tanzanian and Bangweulu cratons (Figure 3.1B; e.g., Corti et al., 2007; Fritz et al., 2013). The RVP is comprised of three volcanoes that have been active in the Quaternary period (Ngozi, Rungwe and Kyejo; black triangles, Figure 3.1B; Fontijn et al., 2010) is highly localized with past eruptions covering ≈1500 km^2 (Figure 3.1B; Ebinger et al., 1989, 1997; Fontijn et al., 2012). ^{40}Ar/^{39}Ar radiometric dating of samples from the RVP suggest that magmatism in the RVP started by 19 Ma (Mesko et al., 2014; 2020) and possibly as early as ≈25 Ma (Roberts et al., 2012).

In this study, we investigate PLI beneath the RVP by using seismic constraints of lithospheric and sublithospheric structures (Fishwick, 2010 updated; Emry et al., 2019) to develop a 3D thermomechanical model of TBC and melt generation beneath the RVP using the finite element code ASPECT (Advanced Solver for Problems in Earth's ConvecTion; Bangerth et al., 2018; Heister et al., 2017; Rose et al., 2017). We approximate a conductive geotherm for the lithosphere with a linear model from the surface to the lithosphere-asthenosphere boundary (LAB), which is defined by the T_p (Rooney et al., 2012). While for the sublithospheric mantle, we approximate an adiabatic increase in temperature with additional temperature perturbations derived from seismic constraints. We assume a rigid lithosphere and apply rheological flow laws that allow for sublithospheric melt generation. TBC has mantle upwelling (≈10 cm/yr) beneath the thin lithosphere of the RVP with associated decompression melting at a maximum depth of ≈200 km consistent with the location and maximum depth (<200 km) of slow P-wave velocity anomalies beneath the RVP (Grijalva et al., 2018; Yu et al., 2020). The seismic constraints indicate excess temperatures in the sublithospheric mantle beneath the RVP that are consistent with the presence of a plume. This work suggests, the presence of a plume is necessary for melt generation beneath the RVP since passive asthenospheric upwelling of ambient mantle requires a higher than normal T_p to generate melt.

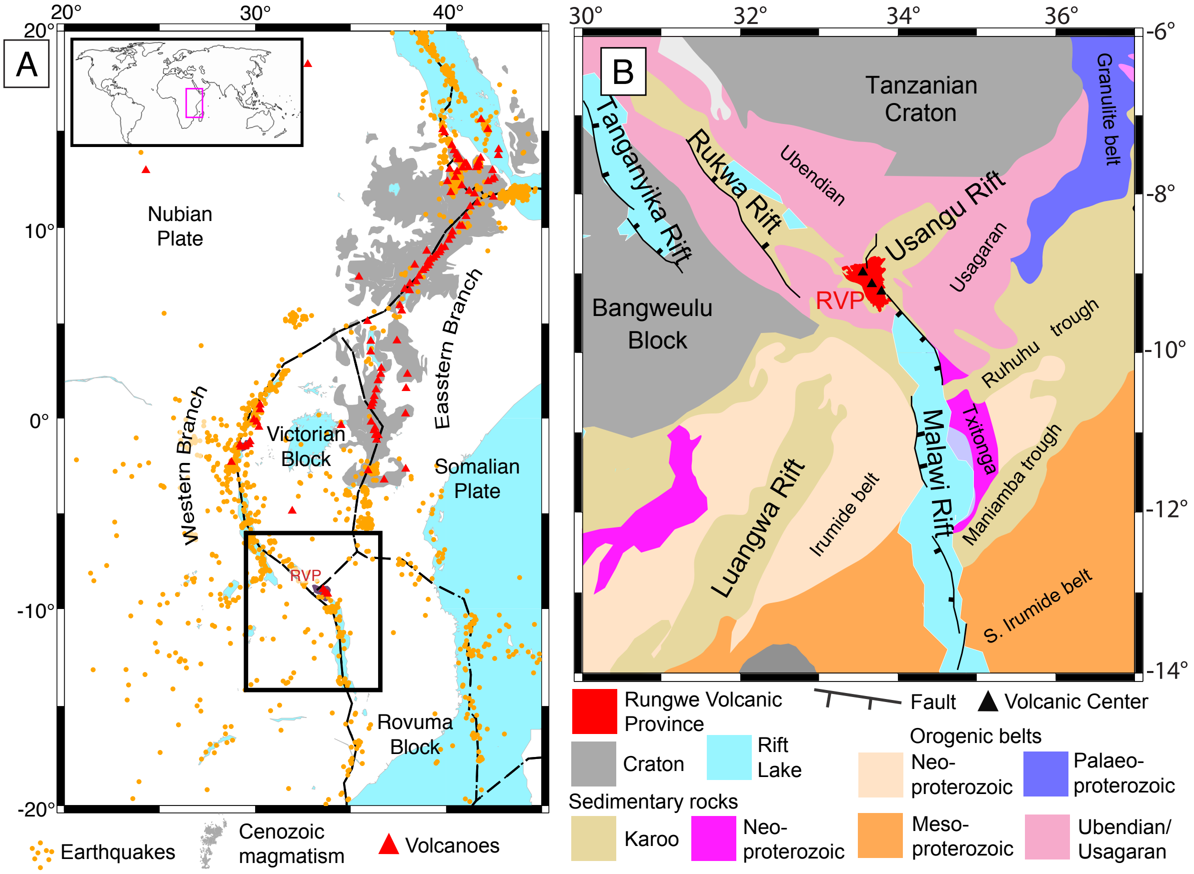

Figure 3.1: (A). Map of the East African Rift (EAR) showing the Eastern and Western Branches. The Western Branch of the EAR has less volcanic centers (red triangles) and more earthquakes (orange dots) than the Eastern Branch. The volcanoes are from the Smithsonian Global Volcanism Project (Siebert et al., 2009) and earthquakes from NEIC catalog (Beauval et al., 2013). The Cenozoic volcanic rocks (gray) after Thiéblemont (2016) indicate the large igneous province (LIP) in the Eastern Branch. RVP = Rungwe Volcanic Province. The black rectangle shows location of Figure 3.1B. Black dotted lines represent plate boundaries from Stamps et al. (2008). The inset map shows the relative location of part of the EAR (pink rectangle) on Earth. (B). Map of major terranes and geological features in the southern part of the Western Branch of the EAR after Fritz et al. (2013). The major rift faults are extracted from Muirhead et al. (2019). Black triangles from north to south represent the three active volcanoes (Ngozi, Rungwe and Kyejo; Fontijn et al., 2010; Harkin, 1960) of the RVP.

3.3 Methods

We simulate time-dependent 3D tomography-based convection (TBC) for 1 Ma that incorporates melt generation in the sublithospheric mantle using ASPECT (Bangerth et al., 2018; Heister et al., 2017; Rose et al., 2017) to test the potential role of PLI in sublithospheric melt generation beneath the RVP. We generate TBC beneath the RVP by solving for the velocity term $\mathbf{u}$ in the Stokes flow equation, which is the conservation equation for momentum (Eq. 3.1) and mass (Eq. 3.2) for an incompressible fluid:

$$-\nabla \cdot [2\eta\, \varepsilon(\mathbf{u})] + \nabla p = \rho \mathbf{g} \qquad \text{in } \Omega, \tag{3.1}$$

$$\nabla \cdot \mathbf{u} = 0 \qquad \text{in } \Omega \tag{3.2}$$

where $\varepsilon(\mathbf{u})$, p, η, ρ, and $\mathbf{g}$ are respectively the strain rate, dynamic pressure field, viscosity, density, and the gravitational acceleration. In order to model melt generation, we also simulate temperature changes in the model by solving the energy conservation equation (Eq. 3.3). We apply the extended Boussinesq approximation that includes adiabatic heating, shear heating, and latent heat of melting in the heating model (Christensen & Yuen, 1985):

$$\begin{aligned} \rho_0 C_p \left(\frac{\partial T}{\partial t} + \mathbf{u} \cdot \nabla T \right) - \nabla \cdot k \nabla T = {} & 2\eta [\varepsilon(\mathbf{u}) : \varepsilon(\mathbf{u})] \\ & + \alpha T \left(\mathbf{u} \cdot \nabla p \right) \\ & + \rho_0 T \Delta S \left(\frac{\partial F}{\partial t} + \mathbf{u} \cdot \nabla F \right) \qquad \text{in } \Omega, \end{aligned} \tag{3.3}$$

where C_p, α, and k are respectively the specific heat capacity, thermal expansivity, thermal conductivity. We assume an average crustal thermal conductivity of $k = 2.5\ W.m^{-1}.K^{-1}$ (Njinju et al., 2019b), $k = 3.5\ W.m^{-1}.K^{-1}$ for the lithospheric mantle (Burov, 2011; Koptev et al., 2018), and $k = 4.7\ W.m^{-1}.K^{-1}$ for the sublithospheric mantle (Clauser & Huenges, 1995; Dannberg & Heister, 2016). The latent heat consumed during melting is implemented in the heating model with an entropy change of $\Delta S =$ -300 $J.kg^{-1}.K^{-1}$ (Dannberg & Heister, 2016). Although we assume incompressibility in the mass conservation equation (Eq. 3.2), the density in the buoyancy term varies with both temperature and pressure:

$$\rho = \rho(T) = \rho_0[1 - \alpha(T - T_0)].e^{\beta(p-p_0)} \tag{3.4}$$

where β is the compressibility coefficient, ρ_0 is the reference density at reference temperature T_0 and reference pressure p_0. We normalize the pressure to a surface pressure of $p_0 = 10^5\ Pa$ (Yang et al., 2018). For the Earth's mantle, $\rho_0 = 3300\ kg/m^3$, $T_0 = 293\ K$, $\alpha = 3 \times 10^{-5}$ K^{-1}, $C_p = 1250\ J.kg^{-1}.K^{-1}$, and $\beta = 4.2 \times 10^{-12}\ Pa^{-1}$.

We use seismically contrained lithospheric structure (Figure 3.2A; Fishwick, 2010 updated) and shear wave velocity perturbations in the sublithospheric mantle (Figure 3.2B; Emry et al., 2019) to define the initial temperature in the model. The lithospheric structure is read from the BALTO site using the BALTO-ASPECT URL reader (Njinju et al., 2020; Stamps et al., 2020). The lithosphere is thinnest beneath the RVP (≈100 km) and thickest beneath the central to southern segment of the Malawi Rift (≈180-200 km). We approximate a conductive geothermal profile for the lithosphere with a linear temperature gradient from the surface ($T_0 = 293\ K$) to the base of the lithosphere. The lithospheric structure produces lateral variations in temperature and pressure such that relatively thin lithosphere has hotter geothermal gradients and lower overburden pressure than the thicker lithosphere and vice versa. The temperature and pressure variations due to variations in the lithospheric thickness lead to lateral density perturbations in the sublithospheric mantle. The initial temperature of the sublithospheric mantle consist of a background temperature that increases approximately adiabatically (0.4 K/km) to the base of the model with additional temperature perturbation derived from shear wave velocity anomalies (Figure 3.2B; Emry et al., 2019). For the Earth's mantle where $\alpha = 3 \times 10^{-5}\ K^{-1}$, $C_p = 1250\ J.kg^{-1}.K^{-1}$, and $g \approx 9.81\ m.s^{-2}$ in the upper mantle for the primary reference earth model (PREM; Dziewonski & Anderson, 1981) which we implement, the adiabatic gradient beneath the RVP is given by:

$$\frac{\partial T}{\partial z} = \frac{\alpha g T_p}{C_p} \approx 0.4\ K/km \tag{3.5}$$

Shear wave velocity perturbation is due to variations in temperature and/or variations in composition. In order to convert the shear wave velocity perturbations to temperature anomalies, we neglect compositional variations and assume that the shear wave velocity anomalies are due to temperature variations only. We first convert the shear wave velocity anomalies to the equivalent density perturbations $\delta\rho/\rho$ using a velocity-density conversion factor of 0.15 (Conrad & Lithgow-Bertelloni, 2006). We multiply the derived density perturbations to the negative inverse of thermal expansivity α (Austermann et al., 2017) to obtain the temperature anomaly dT (Figure 3.2C). The excess temperature at the lithosphere-asthenosphere boundary (LAB) beneath the RVP is ≈80 K (Figure 3.2C). However, geochemical observations of past 10 Ma eruptions in the RVP suggest that the T_p in the RVP is ≈1420°C (≈1693 K; Rooney et al., 2012). Since T_p ≈1693 K beneath the RVP (Rooney et al., 2012), we implement a reference LAB temperature of ≈1613 K in the model.

The initial temperature structure (Figures 3.3A and 3.3B) is therefore the sum of the temperature anomalies due to lateral variations in lithospheric structure and temperature anomalies converted from shear wave velocity anomalies (Figure 3.2B; Emry et al., 2019).

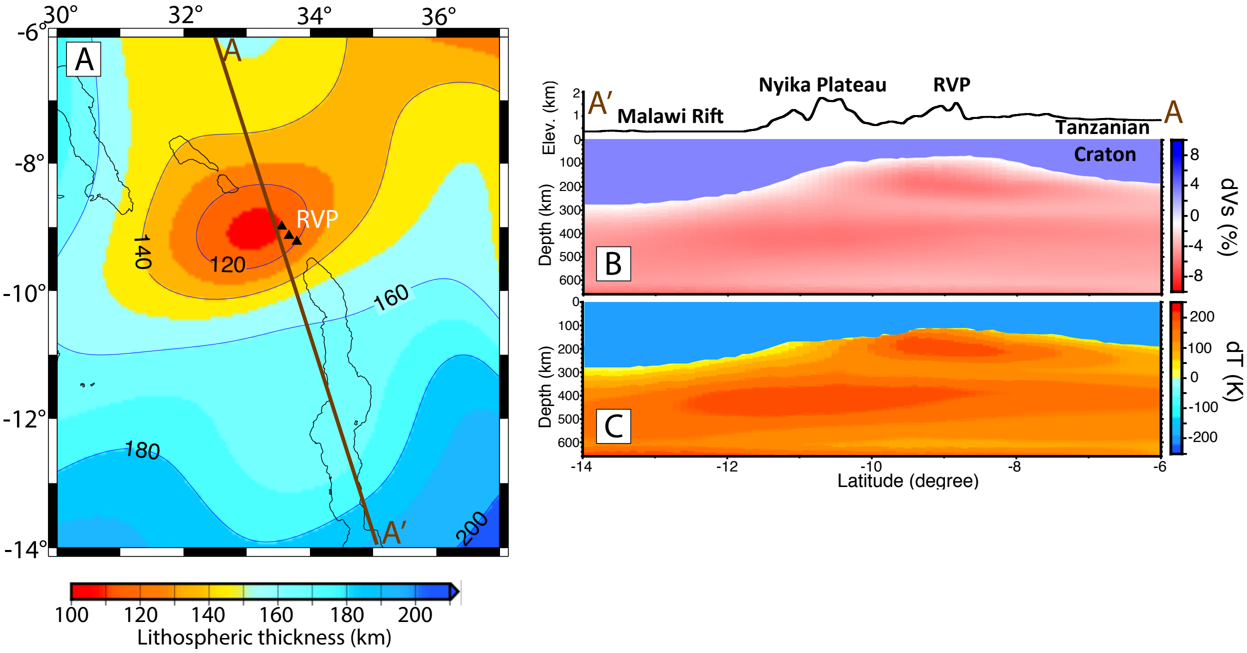

Figure 3.2: (A) Lithospheric thickness map of the Rungwe Volcanic Province (RVP, black triangles) and surroundings, updated from Fishwick (2010) which we use as input in this study. The blue contours show lines of equal lithospheric thickness at 20 km intervals. Black outlines indicate rift lakes. Brown line AA' is the profile location for Figures 3.2B and 3.2C. (B) Cross section of seismic velocity perturbation after Emry et al. (2019). The velocities are relative to the AK135 global average Earth Model (Kennett et al., 1995). (C) Temperature perturbation derived from the velocity perturbation in Figure 3.2B.

Our model domain has dimensions of 800 × 900 × 660 km along latitude, longitude, and depth, respectively, for a spherical chunk geometry (Figure 3.3A). We refine the entire model domain to a global mesh refinement of 6 such that each element is $\approx 12 \times 14 \times 10$ km with 17.5 million unknowns computed on 120 cores. We set the velocities at all the sides of the model to zero, which exerts minimal edge-effects on the model interior from the boundaries of the model. We make the temperature boundary conditions fixed at all boundaries so that the net heat flux at the boundaries is zero following Rajaonarison et al. (2020).

Mantle convection is highly dependent on the viscosity. We impose a strong, uniform viscosity of 10^{23} $Pa.s$ for the lithosphere (Figure 3.3C). For the sublithospheric mantle, we use non-Newtonian, temperature-, pressure- and porosity-dependent creep laws of anhydrous peridotite. The viscosity of the sublithospheric mantle ($\eta_{\text{sublitho-mantle}}$) is given by the multiplication of a porosity dependence factor to a background viscosity governed by composite rheology for dry olivine material parameters (Jadamec & Billen, 2010; Rajaonarison et al., 2020). The composite rheology (η_{comp}) is the harmonic average of the viscosity from dislocation-creep (η_{disl}) and diffusion-creep (η_{diff}) flow laws of dry olivine:

$$\eta_{\text{diff, disl}} = \frac{1}{2} A^{-\frac{1}{n}} d^{\frac{m}{n}} \dot{\epsilon}^{\frac{1-n}{n}} \exp\left(\frac{E_a + pV_a}{nRT}\right) \tag{3.6}$$

$$\eta_{\text{comp}} = \frac{\eta_{\text{diff}} . \eta_{\text{disl}}}{\eta_{\text{diff}} + \eta_{\text{disl}}} \tag{3.7}$$

$$\eta_{\text{sublitho-mantle}} = \eta_{\text{comp}} . e^{-\alpha_{\Phi} \Phi} \tag{3.8}$$

where A is the prefactor, n is the stress exponent, $\dot{\epsilon}$ is the square root of the second invariant of the deviatoric strain rate tensor, d is the grain size, m is the grain size exponent, E_a is the activation energy, V_a is the activation volume, p is pressure, R is the gas constant and, T is the temperature . The values for the parameters A, n, m, E_a and V_a are obtained from experimental studies of dry olivine (Hirth & Kolhstedt, 2003; Table 3.1). The exponential melt-weakening factor is experimentally constrained to $25 \leq \alpha_\Phi \leq 30$ (Mei et al., 2002). We use $\alpha_\Phi = 27$ (Dannberg & Heister, 2016). The porosity Φ is the ratio of the volume of pore spaces between the olivine grains of peridotite to the bulk volume of the peridotite constituent of the asthenosphere. The material properties for each layer (lithosphere and sublithospheric mantle) are implemented as compositional fields with the sublithospheric mantle further divided into two compositional fields called "porosity" and "peridotite". The viscosity at each quadrature point is calculated from the harmonic average of the compositional fields weighted by the volume fraction of each composition at the same location (Figure 3.3C).

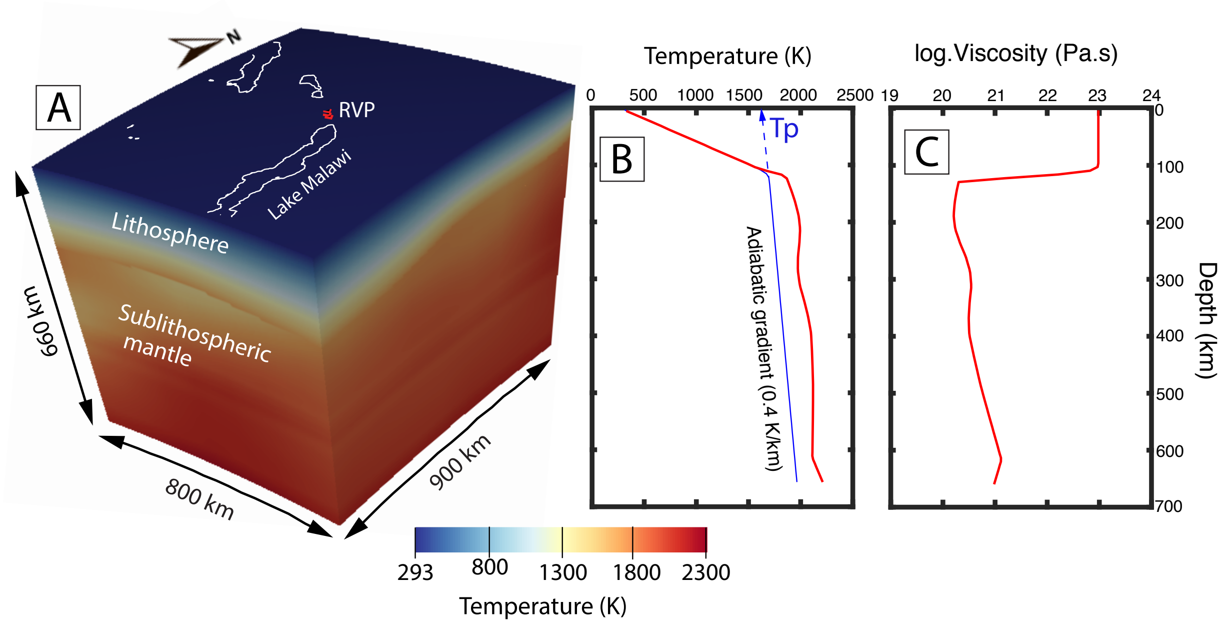

Figure 3.3: (A) Numerical model setup showing the model dimensions and the initial temperature condition as the background in 3D. Red triangles represent the RVP. White lines show the outline of rift lakes. (B) Initial temperature-depth profile beneath the RVP (red line). Blue line represents the 0.4 K/km adiabat. T_p = mantle potential temperature. (C) One-dimensional initial viscosity depth profile beneath the RVP.

We model melt generation in the sublithospheric mantle using the melting model of anhy-

Table 3.1: Rheological Parameters for Dry Olivine Used in the Viscosity Flow Law of the Sublithospheric Mantle

Parameter	Symbol	Dislocation creep	Diffusion creep	Unit
Activation energy	Ea	530 x 10^3	375 x 10^3	J/mol
Activation volume	Va	18 x 10^{-6}	6 x 10^{-6}	m^3/mol
Grain size	d	-	10 x 10^{-3}	m
Grain size exponent	m	-	3	-
Stress exponent	n	3.5	1.0	-
Prefactor	A	7.4 x 10^{-15}	4.5 x 10^{-15}	$Pa^{-n}m^m s^{-1}$

The rheological parameters for the sublithospheric mantle are from Hirth & Kohlstedt (2003). The prefactor in Hirth & Kohlstedt (2003) (i.e. A') is derived from uniaxial strain experiments and is converted to the plane strain equivalent (i.e. A) using the following relationships: $A = \frac{3^{(n+1)/2}}{2^{1-n}} \times 10^{-6(m+n)} A'$, for dry olivine (Becker, 2006).

drous peridotite (Katz et al., 2003), which is valid for shallow upper mantle melting beneath continental lithosphere. Partial melting in the sublithospheric mantle occurs if an adiabatically ascending mantle intersects the solidus. The derived melt fraction $F(p, T)$ depends on the lithostatic pressure p (Pa) and temperature T (K) and is given by:

$$F(p, T) = \left(\frac{T - T_{\text{solidus}}}{T_{\text{liquidus}} - T_{\text{solidus}}} \right)^{1.5}, T_{\text{solidus}} \leq T \leq T_{\text{liquidus}} \tag{3.9}$$

where the mantle solidus temperature T_{solidus} and liquidus temperature T_{liquidus} are respectively given by:

$$T_{\text{solidus}} = A_1 + A_2 p + A_3 p^2 \tag{3.10}$$

$$T_{\text{liquidus}} = B_1 + B_2 p + B_3 p^2 \tag{3.11}$$

where $A_1 = 1085.7\ K$, $A_2 = 1.329 \times 10^{-7}\ K/Pa$, $A_3 = -5.1 \times 10^{-18} K/Pa^2$,

$B_1 = 1475.0\ K$, $B_2 = 8.0 \times 10^{-8}\ K/Pa$, and $B_3 = -3.2 \times 10^{-18} K/Pa^2$.

3.4 Results

In our numerical model, TBC in the sublithospheric mantle arises from our initial temperature conditions. The lithosphere, which is made rigid in the model by imposing a high viscosity ($10^{23} Pa.s$), is not deforming. Since the input seismic constraints (Emry et al., 2019) are static, we run the model for a few time-steps (0-150 Ka) until melt is generated. The time evolution of the melting model (Figure 3.4) indicates that melt generation due to TBC begins at $\approx 75\ Ka$ and the maximum melt fraction peaks ($\approx$0.25 %) at $\approx 130\ Ka$, during which TBC produces strong upwelling that entrains deep, hot mantle materials to shallow, sublithospheric depths. We therefore focus the interpretation of the TBC at 130 Ka. Figures 3.5A and 3.5B show sublithospheric mantle flow patterns at 130 Ka resulting from our numerical modeling of TBC at 150 km and 250 km depth slices, respectively. Mantle upwelling occurs beneath the thin lithosphere of the RVP, while downwelling occurs beneath the relatively thick lithosphere of the surrounding cratons. At 150 km depth (Figure 3.5A), the sublithospheric mantle upwelling ($\approx$2.5 cm/yr) is focused beneath the RVP where the lithosphere is thin ($\approx$100-120 km) with a characteristic radial horizontal mantle flow ($\approx$10 cm/yr). At 250 km depth (Figure 3.5B), the horizontal mantle flow ($\approx$7.5 cm/yr) is characterized by a southwest-ward flow between and around the thick cratonic keels of the Tanzanian and Bangweulu Cratons. The horizontal mantle flow stagnates beneath the RVP where there is rapid mantle upwelling ($\approx$10 cm/yr). This mantle flow pattern is consistent with earlier interpretation from seismic studies by Grijalva et al. (2018).

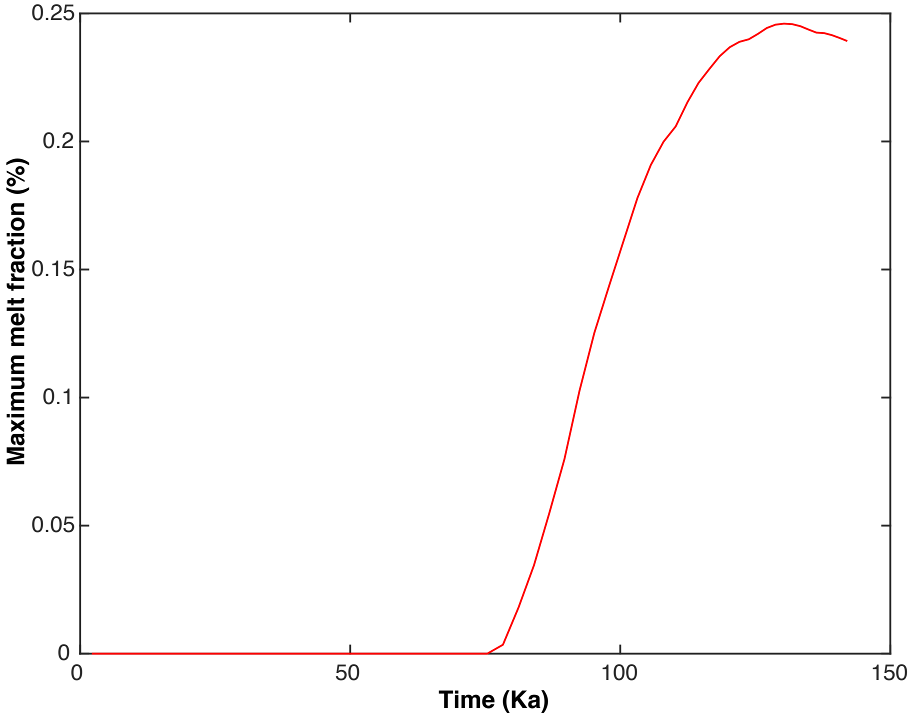

Figure 3.4: A plot of melt fraction versus time showing the evolution of melt in the model. Melt generation due to TBC begins at $\approx 75\ Ka$ and the maximum melt fraction peaks ($\approx$0.25 %) at $\approx 130\ Ka$, during which TBC produces strong upwelling that entrains deep, hot mantle materials to shallow, sublithospheric depths.

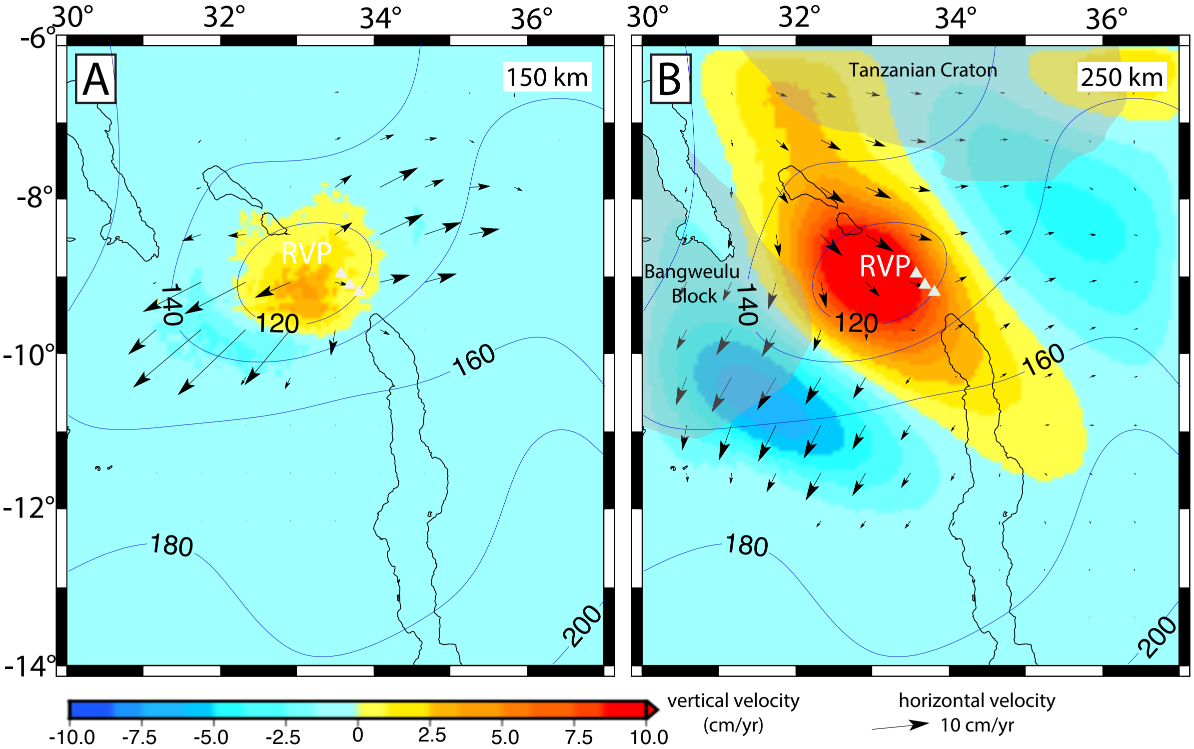

Figure 3.5: Depth slices showing tomography-based convection (TBC) for a model with lateral variations in lithospheric thickness at 130 Ka beneath the RVP at (A) 150 km and (B) 250 km depth. The vertical flow (background color) is overlain by the horizontal flow field (black arrows). White and red triangles in Figures 3.5A and 3.5B respectively represent the RVP. The transparent gray features in Figure 3.5B indicate cratons from Fritz et al. (2013). Blue contours show lines of equal lithospheric thickness at 20 km intervals from Fishwick (2010, updated). Black lines indicate the outline of rift lakes.

Figures 3.6A, and 3.6B respectively show TBC and melt generation for 0 Ka and 130 Ka for the melting parameterization of peridotite (Katz et al., 2003) across the RVP and the long axis of the Malawi Rift (profile AA' is defined in Figure 3.2A). Melt generation due to TBC is restricted to depths of ≈ 100–200 km beneath the RVP where the lithospheric thickness is ≈100 km. Depth slices of the melt model with laterally varying lithospheric thickness at 130 Ka (Figures 3.4A, 3.4B, 3.4C and 3.4D) indicate that melt generation due to TBC is restricted to depths of ≈ 100–200 km beneath the RVP. TBC in the sublithospheric mantle develops (0 Ka; Figure 3.6A) from our initial temperature structure producing mantle upwelling that is focused beneath the thin lithosphere of the RVP. At 0 Ka (Figure 3.6A), melt has yet to generate because the TBC has not evolved enough to entrain deep, hot mantle materials to shallow sublithospheric depths. At 130 Ka (Figure 3.6B), upwelling from the TBC entrains the deep anomalously hot mantle materials beneath the Nyika Plateau (Figure 3.2C) towards shallower depths beneath the RVP, raising the sublithospheric geotherm further to produce more decompression melts.

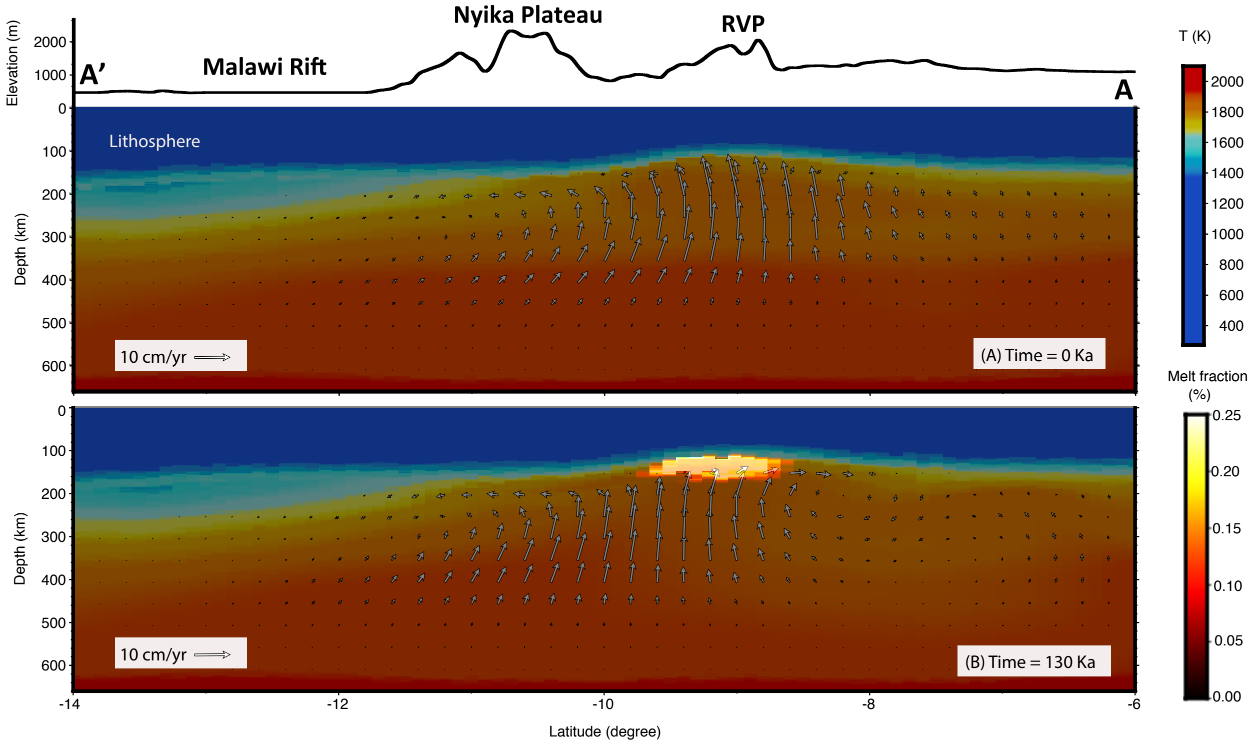

Figure 3.6: Profile showing time-dependent tomography-based convection (TBC) across the Rungwe Volcanic Province (RVP)(profile AA'; Figure 3.2A). (A) Time = 0 Ka. (B) Time = 130 Ka. The temperature field (background color) is overlain by the sublithospheric mantle flow field (arrows).

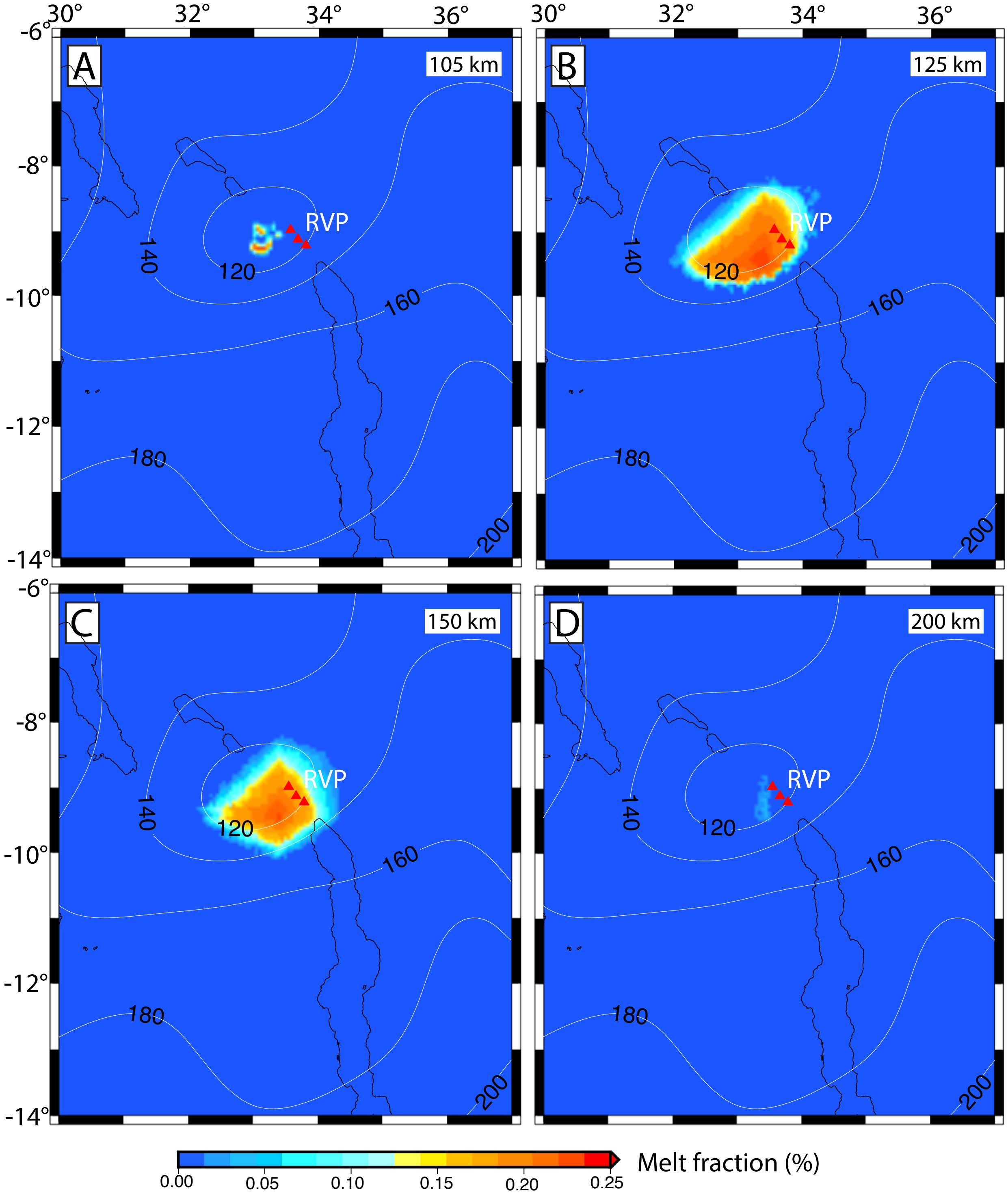

Figure 3.7: Depth slices showing melt fractions beneath the RVP and the Malawi Rift at (A) 105 km, (B) 125 km, (C) 150 km, and (D) 200 km depth at 130 Ka. Red triangles represent the RVP. Black outlines indicate rift lakes. White contours show lines of equal lithospheric thickness at 20 km intervals from Fishwick (2010, updated).

3.5 Discussion

Tomography-Based Convection and Melt Generation

The most prominent features in our model are the isolated region of sublithospheric mantle upwelling and localized decompression melting due to TBC beneath the RVP at depths of $\approx$ 100–200 km. The melting region is spatially consistent with a pronounced low velocity anomaly (LVA) beneath the RVP imaged from P-wave tomography (Grijalva et al., 2018; Yu et al., 2020). The positive temperature anomalies ($\approx 250\ K$) in the sublithospheric mantle beneath the RVP and the Nyika Plateau (Figure 3.2C) might suggest the presence of plume head materials beneath the RVP. The excess temperature of mantle plume heads based on petrological studies is $\approx 200 - 300\ K$ (Schilling, 1991). Thus the LVA beneath the RVP may be a consequence of partial melts generated from a rising plume head that is deflected by the cratonic keels of the Tanzanian and Bangweulu Cratons to focus beneath the thin lithosphere of the RVP as earlier suggested by Grijalva et al. (2018). The shear wave velocity anomalies (Emry et al., 2019) suggest a deeper lithosphere with sharper variations in thickness beneath the RVP and surroundings than the lithospheric thickness from Fishwick (2010 updated) (Figure 3.6A). The sharp variations in the lithospheric thickness beneath the RVP and the surrounding cratons might explain why the magmatism in the RVP is highly localized compared to the LIPs in the Eastern Branch of the EAR (Ayalew et al., 2009) where the lithospheric thickness variation is more gentle (Fishwick, 2010 updated).

Geochemical studies of lava and tephra samples from the RVP by Hilton et al. (2011) shows significantly elevated ^{3}He/^{4}He of 15 RA ($RA =$ air ^{3}He/^{4}He) which far exceeds typical upper mantle values. The high ^{3}He/^{4}He ratios associated with the RVP could be sourced from the primordial mantle in the core-mantle boundary brought to the surface by upwelling mantle plumes (Courtillot et al., 2003). The high mantle potential temperature (1693-1723 K; Rooney et al., 2012) beneath the RVP is another indication of a hot plume material beneath the RVP. Although melt migration in the lithosphere is beyond the scope of this study, the generated sublithospheric melt may subsequently, be injected into the mantle lithosphere and crust through the deep anastomosing structure of the overlying lithospheric scale Mughese Shear Zone. Indeed, Accardo et al. (2020) used local measurements of Rayleigh-wave phase velocities to invert for shear wave velocities and clearly observed low velocities ($<4.3\ km/s$) beneath the RVP at crust and upper-mantle depths that are consistent with the presence of injected magma. The migration of sublithospheric melt to shallower crustal depths suggests a possible mechanism by which plume-sourced melt might finally reach the surface where it erupts producing lava with the observable plume signatures.

3.6 Conclusions

In this study, we develop a 3D thermomechanical model of tomography-based convection (TBC) beneath the Rungwe Volcanic Province (RVP) that incorporates melt generation. We assume a conductive geotherm for the lithosphere while for the sublithospheric mantle, we approximate an adiabatic increase in temperature with additional temperature perturbations derived from seismic constraints. We assume a rigid lithosphere, while for the sublithospheric mantle, we use non-Newtonian, porosity-dependent creep laws of anhydrous peridotite. The seismic constraints indicate excess temperatures of $\approx 250K$ in the sublithospheric mantle beneath the RVP suggesting the presence of a plume. Our TBC simulation is characterized by an isolated sublithospheric mantle upwelling beneath the RVP, which generates decompression melt (≈ 0.25 % melt). Results of our TBC suggest plume head materials might be a source of deep melt for the RVP which explains the high ^{3}He/^{4}He values in their volcanic materials and the elevated mantle potential temperatures. Sharp variation in the lithospheric thickness beneath the RVP and the surrounding cratons might explain why the magmatism in the RVP is highly localized compared to the large igneous provinces in the Eastern Branch of the East African Rift. We conclude that excess temperature from plume materials is necessary for melt generation beneath the RVP because passive asthenospheric upwelling of ambient mantle will require a higher than normal T_p to generate melt.

Acknowledgments

This project is supported by the NSF EarthCube Integration grant 1740627. Most of the figures in this paper were generated with Generic Mapping Tools V5.4.2 (Wessel et al., 2013). We also created a few figures with VISIT v2.9 developed by the Lawrence Livermore National Laboratory. The lithospheric thickness file can be accessed from the BALTO server through the the URL http://balto.opendap.org/opendap/lithosphere_thickness/. We thank the Computational Infrastructure for Geodynamics for supporting the development of ASPECT, which is funded by National Science Foundation Awards EAR-0949446 and EAR-1550901.

Bibliography

Accardo, N., Gaherty, J., Shillington, D., Ebinger, C., Nyblade, A. A., Mbogoni, G., Chindandali, P., Ferdinand, R., Mulibo, G., Kamihanda, G., et al. (2017). Surface wave imaging of the weakly extended malawi rift from ambient-noise and teleseismic rayleigh waves from onshore and lake-bottom seismometers. *Geophysical Journal International*, *209*(3), 1892–1905.

Accardo, N., Gaherty, J., Shillington, D., Hopper, E., Nyblade, A., Ebinger, C., Scholz, C., Chindandali, P., Wambura-Ferdinand, R., Mbogoni, G., et al. (2020). Thermochemical modification of the upper mantle beneath the northern malawi rift constrained from shear velocity imaging. *Geochemistry, Geophysics, Geosystems*, *21*(6), e2019GC008843.

Austermann, J., Mitrovica, J. X., Huybers, P., & Rovere, A. (2017). Detection of a dynamic topography signal in last interglacial sea-level records. *Science Advances*, *3*(7), e1700457.

Ayalew, D., & Gibson, S. A. (2009). Head-to-tail transition of the afar mantle plume: Geochemical evidence from a miocene bimodal basalt–rhyolite succession in the ethiopian large igneous province. *Lithos*, *112*(3-4), 461–476.

Ballmer, M., Van Hunen, J., Ito, G., Tackley, P., & Bianco, T. (2007). Non-hotspot volcano chains originating from small-scale sublithospheric convection. *Geophysical Research Letters*, *34*(23).

Bangerth, W., Dannberg, J., Gassmoeller, R., Heister, T., et al. (2018). ASPECT v2.0.1 [software]. *Computational Infrastructure for Geodynamics*. https://doi.org/10.5281/zenodo.1297145

Bastow, I. D., & Keir, D. (2011). The protracted development of the continent–ocean transition in afar. *Nature Geoscience*, *4*(4), 248–250.

Beauval, C., Yepes, H., Palacios, P., Segovia, M., Alvarado, A., Font, Y., Aguilar, J., Troncoso, L., & Vaca, S. (2013). An earthquake catalog for seismic hazard assessment in ecuador. *Bulletin of the Seismological Society of America*, *103*(2A), 773–786.

Becker, T. W. (2006). On the effect of temperature and strain-rate dependent viscosity on global mantle flow, net rotation, and plate-driving forces. *Geophysical Journal International*, *167*(2), 943–957.

Betzler, C., & Ring, U. (1995). Sedimentology of the malawi rift: Facies and stratigraphy of the chiwondo beds, northern malawi. *Journal of Human Evolution*, *28*(1), 23–35.

Biggs, J., Nissen, E., Craig, T., Jackson, J., & Robinson, D. (2010). Breaking up the hanging wall of a rift-border fault: The 2009 karonga earthquakes, malawi. *Geophysical Research Letters*, *37*(11).

Borrego, D., Nyblade, A. A., Accardo, N. J., Gaherty, J. B., Ebinger, C. J., Shillington, D. J., Chindandali, P. R., Mbogoni, G., Ferdinand, R. W., Mulibo, G., et al. (2018). Crustal structure surrounding the northern malawi rift and beneath the rungwe volcanic province, east africa. *Geophysical Journal International*, *215*(2), 1410–1426.

Buck, W. (2006). The role of magma in the development of the afro-arabian rift system. *Geological Society, London, Special Publications*, *259*(1), 43–54.

Burke, K., & Dewey, J. (1973). Plume-generated triple junctions: Key indicators in applying plate tectonics to old rocks. *The Journal of Geology*, *81*(4), 406–433.

Burov, E. B. (2011). Rheology and strength of the lithosphere. *Marine and Petroleum Geology*, *28*(8), 1402–1443.

Castaing, C. (1991). Post-pan-african tectonic evolution of south malawi in relation to the karroo and recent east african rift systems. *Tectonophysics*, *191*(1-2), 55–73.

Christensen, U. R., & Yuen, D. A. (1985). Layered convection induced by phase transitions. *Journal of Geophysical Research: Solid Earth*, *90*(B12), 10291–10300.

Clauser, C., & Huenges, E. (1995). Thermal conductivity of rocks and minerals. *Rock physics and phase relations: a handbook of physical constants*, *3*, 105–126.

Conrad, C. P., & Lithgow-Bertelloni, C. (2006). Influence of continental roots and asthenosphere on plate-mantle coupling. *Geophysical Research Letters*, *33*(5).

Contreras, J., Anders, M. H., & Scholz, C. H. (2000). Growth of a normal fault system: Observations from the lake malawi basin of the east african rift. *Journal of Structural Geology*, *22*(2), 159–168.

Corti, G., van Wijk, J., Cloetingh, S., & Morley, C. K. (2007). Tectonic inheritance and continental rift architecture: Numerical and analogue models of the east african rift system. *Tectonics*, *26*(6).

Courtillot, V., Davaille, A., Besse, J., & Stock, J. (2003). Three distinct types of hotspots in the earth's mantle. *Earth and Planetary Science Letters*, *205*(3-4), 295–308.

Craig, T., Jackson, J., Priestley, K., & McKenzie, D. (2011). Earthquake distribution patterns in africa: Their relationship to variations in lithospheric and geological structure, and their rheological implications. *Geophysical Journal International*, *185*(1), 403–434.

Crisp, J. A. (1984). Rates of magma emplacement and volcanic output. *Journal of Volcanology and Geothermal Research*, *20*(3-4), 177–211.

DAAC, L. (2004). Global 30 arc-second elevation data set gtopo30. land process distributed active archive center.

Daly, M., Chorowicz, J., & Fairhead, J. (1989). Rift basin evolution in africa: The influence of reactivated steep basement shear zones. *Geological Society, London, Special Publications*, *44*(1), 309–334.

Dannberg, J., Gassmöller, R., Grove, R., & Heister, T. (2019). A new formulation for coupled magma/mantle dynamics. *Geophysical Journal International*, *219*(1), 94–107.

Dannberg, J., & Heister, T. (2016). Compressible magma/mantle dynamics: 3-d, adaptive simulations in aspect. *Geophysical Journal International*, *207*(3), 1343–1366.

Dawson, S. M., Laó-Dávila, D. A., Atekwana, E. A., & Abdelsalam, M. G. (2018). The influence of the precambrian mughese shear zone structures on strain accommodation in the northern malawi rift. *Tectonophysics*, *722*, 53–68.

De Waele, B., Kampunzu, A., Mapani, B., & Tembo, F. (2006). The mesoproterozoic irumide belt of zambia. *Journal of African Earth Sciences*, *46*(1-2), 36–70.

Delvaux, D., Kervyn, F., Macheyeki, A., & Temu, E. (2012). Geodynamic significance of the trm segment in the east african rift (w-tanzania): Active tectonics and paleostress in the ufipa plateau and rukwa basin. *Journal of Structural Geology*, *37*, 161–180.

Dziewonski, A. M., & Anderson, D. L. (1981). Preliminary reference earth model. *Physics of the earth and planetary interiors*, *25*(4), 297–356.

Ebinger, C., Djomani, Y. P., Mbede, E., Foster, A., & Dawson, J. (1997). Rifting archaean lithosphere: The eyasi-manyara-natron rifts, east africa. *Journal of the Geological Society*, *154*(6), 947–960.

Ebinger, C. J., Deino, A. L., Drake, R., & Tesha, A. (1989). Chronology of volcanism and rift basin propagation: Rungwe volcanic province, east africa. *Journal of Geophysical Research: Solid Earth*, *94*(B11), 15785–15803.

Ebinger, C., Deino, A., Tesha, A., Becker, T., & Ring, U. (1993). Tectonic controls on rift basin morphology: Evolution of the northern malawi (nyasa) rift. *Journal of Geophysical Research: Solid Earth*, *98*(B10), 17821–17836.

Ebinger, C., Oliva, S. J., Pham, T.-Q., Peterson, K., Chindandali, P., Illsley-Kemp, F., Drooff, C., Shillington, D. J., Accardo, N. J., Gallacher, R. J., et al. (2019). Kinematics of active deformation in the malawi rift and rungwe volcanic province, africa. *Geochemistry, Geophysics, Geosystems*, *20*(8), 3928–3951.

Ebinger, C. (2005). Continental break-up: The east african perspective. *Astronomy & Geophysics*, *46*(2), 2–16.

Ebinger, C. J., Rosendahl, B., & Reynolds, D. (1987). Tectonic model of the malaŵi rift, africa. *Tectonophysics*, *141*(1-3), 215–235.

Emry, E. L., Shen, Y., Nyblade, A. A., Flinders, A., & Bao, X. (2019). Upper mantle earth structure in africa from full-wave ambient noise tomography. *Geochemistry, Geophysics, Geosystems*, *20*(1), 120–147.

Fagereng, Å. (2013). Fault segmentation, deep rift earthquakes and crustal rheology: Insights from the 2009 karonga sequence and seismicity in the rukwa–malawi rift zone. *Tectonophysics*, *601*, 216–225.

Farr, T. G., Rosen, P. A., Caro, E., Crippen, R., Duren, R., Hensley, S., Kobrick, M., Paller, M., Rodriguez, E., Roth, L., et al. (2007). The shuttle radar topography mission. *Reviews of geophysics*, *45*(2).

Fishwick, S. (2010). Surface wave tomography: Imaging of the lithosphere–asthenosphere boundary beneath central and southern africa? *Lithos*, *120*(1-2), 63–73.

Flannery, J., & Rosendahl, B. (1990). The seismic stratigraphy of lake malawi, africa: Implications for interpreting geological processes in lacustrine rifts. *Journal of African Earth Sciences (and the Middle East)*, *10*(3), 519–548.

Fontijn, K., Ernst, G. G., Elburg, M. A., Williamson, D., Abdallah, E., Kwelwa, S., Mbede, E., & Jacobs, P. (2010). Holocene explosive eruptions in the rungwe volcanic province, tanzania. *Journal of volcanology and geothermal research*, *196*(1-2), 91–110.

Fontijn, K., Williamson, D., Mbede, E., & Ernst, G. G. (2012). The rungwe volcanic province, tanzania–a volcanological review. *Journal of African Earth Sciences*, *63*, 12–31.

Fritz, H., Abdelsalam, M., Ali, K., Bingen, B., Collins, A., Fowler, A., Ghebreab, W., Hauzenberger, C., Johnson, P., Kusky, T., et al. (2013). Orogen styles in the east african orogen: A review of the neoproterozoic to cambrian tectonic evolution. *Journal of African Earth Sciences*, *86*, 65–106.

Furman, T., Kaleta, K. M., Bryce, J. G., & Hanan, B. B. (2006). Tertiary mafic lavas of turkana, kenya: Constraints on east african plume structure and the occurrence of high-μ volcanism in africa. *Journal of Petrology*, *47*(6), 1221–1244.

Gaherty, J., Zheng, W., Shillington, D., Pritchard, M., Henderson, S., Chindandali, P., Mdala, H., Shuler, A., Lindsey, N., Oliva, S., et al. (2019). Faulting processes during early-stage rifting: Seismic and geodetic analysis of the 2009–2010 northern malawi earthquake sequence. *Geophysical Journal International*, *217*(3), 1767–1782.

Gallagher, J., Potter, N., Sgouros, T., Hankin, S., & Flierl, G. (2004). The data access protocol—dap 2.0. *http://www. opendap. org/.*

Giacomo, A. M. A. (1984). Petrochemistry, tectonic evolution and metasomatic mineralisations of mozambique belt granulites from s malawi and tete (mozambique). *Precambrian Research*, *25*(1-3), 161–186.

Grijalva, A., Nyblade, A. A., Homman, K., Accardo, N. J., Gaherty, J. B., Ebinger, C. J., Shillington, D. J., Chindandali, P. R., Mbogoni, G., Ferdinand, R. W., et al. (2018). Seismic evidence for plume-and craton-influenced upper mantle structure beneath the northern malawi rift and the rungwe volcanic province, east africa. *Geochemistry, Geophysics, Geosystems*, *19*(10), 3980–3994.

Hanson, R. E., Wilson, T. J., & Munyanyiwa, H. (1994). Geologic evolution of the neoproterozoic zambezi orogenic belt in zambia. *Journal of African Earth Sciences*, *18*(2), 135–150.

Hargrove, U. S., Hanson, R. E., Martin, M. W., Blenkinsop, T. G., Bowring, S. A., Walker, N., & Munyanyiwa, H. (2003). Tectonic evolution of the zambezi orogenic belt: Geochronological, structural, and petrological constraints from northern zimbabwe. *Precambrian Research*, *123*(2-4), 159–186.

Harkin, D. A. (1960). The rungwe volcanics at the northern end of lake nyasa.

Heilman, E., Kolawole, F., Atekwana, E. A., & Mayle, M. (2019). Controls of basement fabric on the linkage of rift segments. *Tectonics*, *38*(4), 1337–1366.

Heister, T., Dannberg, J., Gassmöller, R., & Bangerth, W. (2017). High accuracy mantle convection simulation through modern numerical methods–ii: Realistic models and problems. *Geophysical Journal International*, *210*(2), 833–851.

Hilbert-Wolf, H., Roberts, E., Downie, B., Mtelela, C., Stevens, N. J., & O'Connor, P. (2017). Application of u–pb detrital zircon geochronology to drill cuttings for age control in hydrocarbon exploration wells: A case study from the rukwa rift basin, tanzania. *AAPG Bulletin*, *101*(2), 143–159.

Hilton, D. R., Halldórsson, S. A., Barry, P. H., Fischer, T., de Moor, J., Ramirez, C., Mangasini, F., & Scarsi, P. (2011). Helium isotopes at rungwe volcanic province, tanzania, and the origin of east african plateaux. *Geophysical Research Letters*, *38*(21).

Hirth, G., & Kohlstedf, D. (2003). Rheology of the upper mantle and the mantle wedge: A view from the experimentalists. *Geophysical Monograph-American Geophysical Union*, *138*, 83–106.

Jackson, J., & Blenkinsop, T. (1997). The bilila-mtakataka fault in malaŵi: An active, 100-km long, normal fault segment in thick seismogenic crust. *Tectonics*, *16*(1), 137–150.

Jadamec, M. A., & Billen, M. I. (2010). Reconciling surface plate motions with rapid three-dimensional mantle flow around a slab edge. *Nature*, *465*(7296), 338–341.

Karato, S.-i., & Wu, P. (1993). Rheology of the upper mantle: A synthesis. *Science*, *260*(5109), 771–778.

Katumwehe, A. B., Abdelsalam, M. G., & Atekwana, E. A. (2015). The role of pre-existing precambrian structures in rift evolution: The albertine and rhino grabens, uganda. *Tectonophysics*, *646*, 117–129.

Katz, R. F., Spiegelman, M., & Langmuir, C. H. (2003). A new parameterization of hydrous mantle melting. *Geochemistry, Geophysics, Geosystems*, *4*(9).

Keller, T., May, D. A., & Kaus, B. J. (2013). Numerical modelling of magma dynamics coupled to tectonic deformation of lithosphere and crust. *Geophysical Journal International*, *195*(3), 1406–1442.

Kendall, J.-M., Stuart, G., Ebinger, C., Bastow, I., & Keir, D. (2005). Magma-assisted rifting in ethiopia. *Nature*, *433*(7022), 146–148.

Kendall, J.-M., & Lithgow-Bertelloni, C. (2016). Why is africa rifting? *Geological Society, London, Special Publications*, *420*(1), 11–30.

Kennett, B. L., Engdahl, E., & Buland, R. (1995). Constraints on seismic velocities in the earth from traveltimes. *Geophysical Journal International*, *122*(1), 108–124.

King, S. D., & Anderson, D. L. (1998). Edge-driven convection. *Earth and Planetary Science Letters*, *160*(3-4), 289–296.

Kolawole, F., Atekwana, E. A., Laó-Dávila, D. A., Abdelsalam, M. G., Chindandali, P. R., Salima, J., & Kalindekafe, L. (2018). Active deformation of malawi rift's north basin hinge zone modulated by reactivation of preexisting precambrian shear zone fabric. *Tectonics*, *37*(3), 683–704.

Koptev, A., Calais, E., Burov, E., Leroy, S., & Gerya, T. (2015). Dual continental rift systems generated by plume–lithosphere interaction. *Nature Geoscience*, *8*(5), 388–392.

Koptev, A., Cloetingh, S., Gerya, T., Calais, E., & Leroy, S. (2018). Non-uniform splitting of a single mantle plume by double cratonic roots: Insight into the origin of the central and southern east african rift system. *Terra Nova*, *30*(2), 125–134.

Kronbichler, M., Heister, T., & Bangerth, W. (2012). High accuracy mantle convection simulation through modern numerical methods. *Geophysical Journal International*, *191*(1), 12–29.

Laó-Dávila, D. A., Al-Salmi, H. S., Abdelsalam, M. G., & Atekwana, E. A. (2015). Hierarchical segmentation of the malawi rift: The influence of inherited lithospheric heterogeneity and kinematics in the evolution of continental rifts. *Tectonics*, *34*(12), 2399–2417.

Leseane, K., Atekwana, E. A., Mickus, K. L., Abdelsalam, M. G., Shemang, E. M., & Atekwana, E. A. (2015). Thermal perturbations beneath the incipient okavango rift zone, northwest botswana. *Journal of Geophysical Research: Solid Earth*, *120*(2), 1210–1228.

McConnell, R. (1972). Geological development of the rift system of eastern africa. *Geological Society of America Bulletin*, *83*(9), 2549–2572.

Mckenzie, D., & Bickle, M. (1988). The volume and composition of melt generated by extension of the lithosphere. *Journal of petrology*, *29*(3), 625–679.

McKenzie, D., & O'NIONS, R. K. (1995). The source regions of ocean island basalts. *Journal of petrology*, *36*(1), 133–159.

Mei, S., Bai, W., Hiraga, T., & Kohlstedt, D. L. (2002). Influence of melt on the creep behavior of olivine–basalt aggregates under hydrous conditions. *Earth and Planetary Science Letters*, *201*(3-4), 491–507.

Mesko, G. (2020). *Magmatism at the southern end of the east african rift system: Origin and role during early stage rifting* (Doctoral dissertation). Columbia University.

Mesko, G., Class, C., Maqway, M., Boniface, N., Manya, S., & Hemming, S. (2014). The timing of early magmatism and extension in the southern east african rift: Tracking geochemical source variability with 40 ar/39 ar geochronology at the rungwe volcanic province, sw tanzania. *AGUFM*, *2014*, V51A–4730.

Morley, C., Haranya, C., Phoosongsee, W., Pongwapee, S., Kornsawan, A., & Wonganan, N. (2004). Activation of rift oblique and rift parallel pre-existing fabrics during extension and their effect on deformation style: Examples from the rifts of thailand. *Journal of Structural Geology*, *26*(10), 1803–1829.

Muirhead, J. D., Wright, L. J., & Scholz, C. A. (2019). Rift evolution in regions of low magma input in east africa. *Earth and Planetary Science Letters*, *506*, 332–346.

Nielsen, T. K., & Hopper, J. R. (2002). Formation of volcanic rifted margins: Are temperature anomalies required? *Geophysical Research Letters*, *29*(21), 18–1.

Njinju, E., Stamps, D. S., Neumiller, K., & Gallagher, J. (2020). Lithospheric control of melt generation beneath the rungwe volcanic province and the malawi rift, east africa.

Njinju, E. A., Atekwana, E. A., Stamps, D. S., Abdelsalam, M. G., Atekwana, E. A., Mickus, K. L., Fishwick, S., Kolawole, F., Rajaonarison, T. A., & Nyalugwe, V. N. (2019). Lithospheric structure of the malawi rift: Implications for magma-poor rifting processes. *Tectonics*, *38*(11), 3835–3853.

Njinju, E. A., Kolawole, F., Atekwana, E. A., Stamps, D. S., Atekwana, E. A., Abdelsalam, M. G., & Mickus, K. L. (2019). Terrestrial heat flow in the malawi rifted zone, east africa: Implications for tectono-thermal inheritance in continental rift basins. *Journal of Volcanology and Geothermal Research*, *387*, 106656.

O'Donnell, J., Adams, A., Nyblade, A. A., Mulibo, G., & Tugume, F. (2013). The uppermost mantle shear wave velocity structure of eastern africa from rayleigh wave tomography: Constraints on rift evolution. *Geophysical Journal International*, *194*(2), 961–978.

Olsen, K. H. (1995). *Continental rifts: Evolution, structure, tectonics*. Elsevier.

Peslier, A., Woodland, A., Bell, D., Lazarov, M., & Lapen, T. (2012). Metasomatic control of water contents in the kaapvaal cratonic mantle. *Geochimica et Cosmochimica Acta*, *97*, 213–246.

Rajaonarison, T. A., Stamps, D. S., Fishwick, S., Brune, S., Glerum, A., & Hu, J. (2020). Numerical modeling of mantle flow beneath madagascar to constrain upper mantle rheology beneath continental regions. *Journal of Geophysical Research. Solid Earth*, *125*(2), Art–No.

Ranalli, G. (1995). *Rheology of the earth*. Springer Science & Business Media.

Reed, C. A., Liu, K. H., Chindandali, P. R., Massingue, B., Mdala, H., Mutamina, D., Yu, Y., & Gao, S. S. (2016). Passive rifting of thick lithosphere in the southern east african rift: Evidence from mantle transition zone discontinuity topography. *Journal of Geophysical Research: Solid Earth*, *121*(11), 8068–8079.

Ring, U. (1994). The influence of preexisting structure on the evolution of the cenozoic malawi rift (east african rift system). *Tectonics*, *13*(2), 313–326.

Ring, U., Kröner, A., Buchwaldt, R., Toulkeridis, T., & Layer, P. W. (2002). Shear-zone patterns and eclogite-facies metamorphism in the mozambique belt of northern malawi, east-central africa: Implications for the assembly of gondwana. *Precambrian Research*, *116*(1-2), 19–56.

Roberts, E. M., Stevens, N., O'Connor, P. M., Dirks, P., Gottfried, M. D., Clyde, W., Armstrong, R., Kemp, A., & Hemming, S. (2012). Initiation of the western branch of the east african rift coeval with the eastern branch. *Nature Geoscience*, *5*(4), 289–294.

Rooney, T. O., Herzberg, C., & Bastow, I. D. (2012). Elevated mantle temperature beneath east africa. *Geology*, *40*(1), 27–30.

Rose, I., Buffett, B., & Heister, T. (2017). Stability and accuracy of free surface time integration in viscous flows. *Physics of the Earth and Planetary Interiors*, *262*, 90–100.

Sacchi, R., Cadoppi, P., & Costa, M. (2000). Pan-african reactivation of the lurio segment of the kibaran belt system: A reappraisal from recent age determinations in northern mozambique. *Journal of African Earth Sciences*, *30*(3), 629–639.

Sarafian, E., Evans, R. L., Abdelsalam, M. G., Atekwana, E., Elsenbeck, J., Jones, A. G., & Chikambwe, E. (2018). Imaging precambrian lithospheric structure in zambia using electromagnetic methods. *Gondwana Research*, *54*, 38–49.

Saria, E., Calais, E., Stamps, D., Delvaux, D., & Hartnady, C. (2014). Present-day kinematics of the east african rift. *Journal of Geophysical Research: Solid Earth*, *119*(4), 3584–3600.

Saunders, A., Storey, M., Kent, R., & Norry, M. (1992). Consequences of plume-lithosphere interactions. *Geological Society, London, Special Publications*, *68*(1), 41–60.

Schilling, J.-G. (1991). Fluxes and excess temperatures of mantle plumes inferred from their interaction with migrating mid-ocean ridges. *Nature*, *352*(6334), 397–403.

Schmeling, H. (2010). Dynamic models of continental rifting with melt generation. *Tectonophysics*, *480*(1-4), 33–47.

Schutt, D. L., & Lesher, C. E. (2010). Compositional trends among kaapvaal craton garnet peridotite xenoliths and their effects on seismic velocity and density. *Earth and Planetary Science Letters*, *300*(3-4), 367–373.

Siebert, L., Simkin, T., & Kimberly, P. (2009). Four-decades perspective on earth's volcanoes by the smithsonian's global volcanism program. *AGUFM*, *2009*, V23I–01.

Specht, T. D., & Rosendahl, B. R. (1989). Architecture of the lake malawi rift, east africa. *Journal of African Earth Sciences (and the Middle East)*, *8*(2-4), 355–382.

Stamps, D. S., Calais, E., Saria, E., Hartnady, C., Nocquet, J.-M., Ebinger, C. J., & Fernandes, R. M. (2008). A kinematic model for the east african rift. *Geophysical Research Letters*, *35*(5).

Stamps, D. S., Gallagher, J., Peckham, S., Sheehan, A., Potter, N., Neumiller, K., Njinju, E., Stoica, M., Easton, Z., Fuka, D., et al. (2020). Seamless long-tail and big data access via the earthcube brokering cyberinfrastructure balto.

Stamps, D., Flesch, L., & Calais, E. (2010). Lithospheric buoyancy forces in africa from a thin sheet approach. *International Journal of Earth Sciences*, *99*(7), 1525–1533.

Stamps, D., Flesch, L., Calais, E., & Ghosh, A. (2014). Current kinematics and dynamics of africa and the east african rift system. *Journal of Geophysical Research: Solid Earth*, *119*(6), 5161–5186.

Thieblemont, D. (2016). An updated geological map of africa at 1/10 000 000 scale.

Thybo, H., & Nielsen, C. A. (2009). Magma-compensated crustal thinning in continental rift zones. *Nature*, *457*(7231), 873–876.

Van Wijk, J. (2005). Role of weak zone orientation in continental lithosphere extension. *Geophysical Research Letters*, *32*(2).

Van Wijk, J., Huismans, R., Ter Voorde, M., & Cloetingh, S. (2001). Melt generation at volcanic continental margins: No need for a mantle plume? *Geophysical Research Letters*, *28*(20), 3995–3998.

Wessel, P., Smith, W. H., Scharroo, R., Luis, J., & Wobbe, F. (2013). Generic mapping tools: Improved version released. *Eos, Transactions American Geophysical Union*, *94*(45), 409–410.

Westerhof, A. P., Lehtonen, M. I., Mäkitie, H., Manninen, T., Pekkala, Y., Gustafsson, B., & Tahon, A. (2008). The tete-chipata belt: A new multiple terrane element from western mozambique and southern zambia. *Geological Survey of Finland Special Paper*, *48*, 145–166.

Wheeler, W. H. (1989). *The livingstone mountains border fault system, lake nyasa (malawi), east africa: A case study of an oblique-slip rift basin border fault from onshore and subsurface perspectives* (Doctoral dissertation). Duke University.

White, R., & McKenzie, D. (1989). Magmatism at rift zones: The generation of volcanic continental margins and flood basalts. *Journal of Geophysical Research: Solid Earth*, *94*(B6), 7685–7729.

Wilson, D., Aster, R., West, M., Ni, J., Grand, S., Gao, W., Baldridge, W. S., Semken, S., & Patel, P. (2005). Lithospheric structure of the rio grande rift. *Nature*, *433*(7028), 851–855.

Yang, H., Chemia, Z., Artemieva, I. M., & Thybo, H. (2018). Control on off-rift magmatism: A case study of the baikal rift zone. *Earth and Planetary Science Letters*, *482*, 501–509.

Yu, Y., Gao, S. S., Zhao, D., & Liu, K. H. (2020). Mantle structure and flow beneath an early-stage continental rift: Constraints from p wave anisotropic tomography. *Tectonics*, *39*(2), e2019TC005590.